Discrete time crystals in Bose-Einstein condensates and the symmetry-breaking edge in a simple two-mode theory

Jia Wang [1,*] Krzysztof Sacha,[2] Peter Hannaford,[3] and Bryan J. Dalton [1,†]

[1]*Centre for Quantum Technology Theory, Swinburne University of Technology, Melbourne 3122, Australia*
[2]*Instytut Fizyki Teoretycznej, Uniwersytet Jagielloński, ulica Profesora Stanislawa Lojasiewicza 11, PL-30-348 Kraków, Poland*
[3]*Optical Sciences Centre, Swinburne University of Technology, Melbourne 3122, Australia*

Discrete time crystals (DTCs) refer to a novel many-body steady state that spontaneously breaks the discrete time-translational symmetry in a periodically driven quantum system. Here, we study DTCs in a Bose-Einstein condensate bouncing resonantly on an oscillating mirror, using a two-mode model derived from a standard quantum field theory. We investigate the validity of this model and apply it to study the long-time behavior of our system. A wide variety of initial states based on two Wannier modes are considered. We find that in previous studies the investigated phenomena in the evolution time window ($\lesssim$2000 driving periods) are actually "short-time" transient behavior though DTC formation signaled by the subharmonic responses is still shown if the interboson interaction is strong enough. After a much longer (about 20 times) evolution time, initial states with no "long-range" correlations relax to a steady state, where time-symmetry breaking can be unambiguously defined. Quantum revivals also eventually occur. This long-time behavior can be understood via the many-body Floquet quasieigenenergy spectrum of the two-mode model. A symmetry-breaking edge for DTC formation appears in the spectrum for strong enough interaction, where all quasieigenstates below the edge are symmetry breaking while those above the edge are symmetric. The late-time steady state's time-translational symmetry depends solely on whether the initial energy is above or below the symmetry-breaking edge. A phase diagram showing regions of symmetry-broken and symmetric phases for differing initial energies and interaction strengths is presented. We find that, according to this two-mode model, the discrete time crystal survives for times out to at least 250 000 driving periods.

I. INTRODUCTION

Traditionally, spontaneous symmetry breaking (SSB) refers to a situation where the ground state or a thermal ensemble at a finite temperature of a many-body system is less symmetrical than its parent Hamiltonian. Breaking of different symmetries plays a profound role in many aspects of physics, including (spatial) crystal formation, magnetism, superconductivity, and the origin of particle masses via the Higgs mechanism. However, spontaneous time-translational symmetry breaking had rarely been considered until Wilczek proposed the controversial concept of a "time crystal" [1]. Wilczek's original proposal, breaking of continuous time-translational symmetry in the ground state (or any thermal equilibrium state), was later rejected by the "no-go" theorem of Watanabe and Oshikawa [2,3]. Nevertheless, physicists have recently demonstrated that spontaneous discrete time-translational symmetry breaking (SDTTSB), i.e., discrete time crystals (DTCs), can exist in out-of-equilibrium systems, such as Floquet systems that are periodic in time with period T [4–7]. Experimental evidence of time crystallinity has been reported recently in a variety of different platforms [8–15].

Discrete time crystals have developed rapidly recently and have attracted a lot of attention [16–23]. Reviews on the topic of time crystals can be found in Refs. [24–27].

However, a generic many-body system under periodic driving would normally keep absorbing energy and approach an infinite-temperature state, a featureless state that cannot support SDTTSB [28–30]. Therefore, the existence of a DTC relies on the prevention (or at least long-time suppression) of Floquet heating to stabilize the nonequilibrium quantum state. Indeed, several innovative mechanisms can help to avoid the heating problem in quantum many-body systems, including many-body localization (MBL) [31–33], prethermalization [34–36], and, more recently, many-body quantum scars [37–40].

On the other hand, generalizing SSB to time-dependent Floquet systems where no well-defined ground state or any thermal equilibrium states exist requires a careful theoretical development [2]. It is now argued that a natural generalization of the equilibrium notion of SSB can be defined via the long-time steady state [26]. Following the nomenclature in [26], steady states in Floquet many-body systems are defined as those with expectation values of local observables that relax to constants at stroboscopic times $t = T$, $2T$, $3T$, ... In the case where time-translational symmetry is broken, we extend the definition to states with constant expectation values of local observables at $t = sT$, $2sT$, $3sT$, ... with s being an

*jiawang@swin.edu.au
†bdalton@swin.edu.au

integer. In a generic many-body system, any short-ranged correlated initial state would usually approach a steady state after some possible transient evolution. Therefore, in isolated quantum systems out of equilibrium, SSB can be defined as the situation where the steady state (in the thermalization limit) is less symmetrical than its parent Hamiltonian. In particular, a DTC refers to the case where the steady state has a period sT that is a multiple s of the drive period T. In the simplest case, for $s = 2$, this amounts to a period doubling or a subharmonic response at $0.5\omega \equiv \pi/T$.

A well-known property of Floquet systems is that a time-independent effective Hamiltonian, namely, the Floquet Hamiltonian H_F, determines the stroboscopic ($t = T, 2T, 3T, \ldots$) dynamics [41–43]. Therefore, the eigenstates and eigenvalues (namely, Floquet states and Floquet energies, respectively) of H_F or its equivalent Floquet evolution operator $U_F \equiv \exp(-iH_F T)$ also encode all the necessary information to define SDTTSB. Indeed, Refs. [44–46] have shown that all eigenstates of U_F for a ($s = 2$) MBL DTC come in pairs with eigenvalues that have a phase difference π, which is associated with the period doubling of the steady state for systems starting with physically relevant initial states. In contrast, only one pair of eigenstates shows the π pairing in a many-body quantum scar system studied in [40].

Here, we revisit the initial proposal [4] that identified the possibility of realizing DTCs in a bouncing Bose-Einstein condensate (BEC) under periodic driving, where not all but an extensive set of eigenstates with eigenvalues under a symmetry-breaking edge come in pairs. This initial work [4] and some of the following studies apply a mean-field approximation [47,48] or a time-dependent Bogoliubov approximation [49], which might artificially preclude or underestimate Floquet heating in this system since only one or a few modes are included. Mean-field theories assume that there is no depletion from the condensate mode, and Bogoliubov theory assumes any depletion is small. As well as allowing for large depletion and allowing for quantum fluctuations, a multimode treatment is needed to examine the possibility of thermalization, as this could prevent DTC formation [25,26]. We recently investigated the case $s = 2$ via a fully comprehensive multimode quantum treatment based on a phase-space many-body approach involving the truncated Wigner approximation (TWA) [50], which can include thermalization effects. However, thermalization is found to be absent in our system, and we find a robust subharmonic response for interactions stronger than some critical value $|g_c N|$ and lasting for a significant period of time, which is a practical criterion of DTC formation commonly adopted [5–7]. Nevertheless, at present, the TWA is limited in the time regime that can be computed due to computation resource constraints.

Interestingly, we find for the parameter regime studied that only two (Wannier) modes were significantly occupied for $s = 2$, suggesting that a many-body theory based on just two dominant modes should work well in this regime [50]. The two-mode model allows us to investigate the dynamics over much longer evolution times. In this long-time regime, the system indeed relaxes to a steady state, where the dynamics is purified and the order parameter for time-symmetry breaking can be unambiguously determined. References [4,49] also developed a beyond-mean-field two-mode model. However,

the approximation adopted in the derivation was not clearly justified. Here, we derive the two-mode model from a standard quantum field theory. We examine the two-mode approximation in comparison with the multimode TWA, and argue that the two-mode approximation for $s = 2$ can be applied to a long evolution time. We also find that the spectrum of this model Hamiltonian determines the behavior and symmetry of the long-time steady state. We note that our two-mode model is not the same as two-mode treatments in mean-field theory (such as in [51]) where the condensate wave function is written as a linear combination of two mode functions. In contrast, our two-mode model includes beyond-mean-field effects and allows atoms to macroscopically occupy more than one mode. We found in our previous multimode TWA treatment that near the critical value of the interaction strength $|g_c N|$ (which corresponds to the onset of DTC formation), the mean-field theory does not provide a good description of the position probability density or one-body projector, nor can it account for depletion from the condensate mode [see Figs. 6, 9(b), 9(f), and 11 in Ref. [50]]. The present two-mode model can account for all of these features.

The paper is organized as follows. In Sec. II we introduce the many-body model for a BEC of bosonic atoms bouncing resonantly on an oscillating mirror and investigate the validity of the two-mode model for the case of $s = 2$ and period doubling. In Sec. III we present details of our two-mode model and calculations of the evolution of the system out to very long times. In Sec. IV we discuss the symmetry breaking in terms of a symmetry-breaking edge of the two-mode Hamiltonian. Our results are summarized in Sec. V. Details and some derivations of equations are given in the Appendices.

II. MANY-BODY MODEL

We consider N bosons bouncing vertically on an oscillating mirror under strong confinement in the transverse directions, which can be regarded as a one-dimensional (1D) system. The quantum dynamics is determined by the many-body Schrödinger equation $i\hbar \partial_t |\Theta(t)\rangle = \hat{H}|\Theta(t)\rangle$, where the Hamiltonian can be written

$$\hat{H} = \int dz \left[\hat{\Psi}(z)^\dagger H_{sp} \hat{\Psi}(z) + \frac{g}{2} \hat{\Psi}(z)^\dagger \hat{\Psi}(z)^\dagger \hat{\Psi}(z) \hat{\Psi}(z) \right], \quad (1)$$

in terms of the field operators $\hat{\Psi}(z)$ and $\hat{\Psi}(z)^\dagger$ for the annihilation and creation of a bosonic atom of mass m at position z. Here, the single-particle Hamiltonian is given by $H_{sp} = -\partial_z^2/2 + V(z,t)$ using gravitational units for convenience, where the length, time, and energy in gravitational units are $l_G = (\hbar^2/m^2 g_E)^{1/3}$, $t_G = (\hbar/m g_E^2)^{1/3}$, and $E_G = m g_E l_G$ with g_E being the gravitational acceleration. (Throughout this work, quantities shown in the figures are either dimensionless or are given in terms of gravitational units.) $g = 2\omega_\perp a_s$ is the 1D coupling constant, where a_s is the s-wave scattering length and $\omega_\perp$ is the oscillation frequency for the BEC atoms in a transverse trap. In the coordinate frame moving with the oscillating mirror (which can be transformed from the laboratory frame via a gauge transformation [4,52]), the temporally periodic potential is given by

$$V(z,t) = z(1 - \lambda \cos \omega t), \quad (2)$$

with $z \geqslant 0$. Here, $\omega = 2\pi/T$ is the driving frequency of the mirror, and T is the corresponding period. The parameter λ determines the driving amplitude. A formal method to solve the single-particle problem is the Floquet formalism, where the T-periodic Floquet eigenenergies ϵ_ν and eigenstates $\phi_\nu(z, t) = \phi_\nu(z, t + T)$ can be defined as

$$[H_{\mathrm{sp}} - i\partial_t]\phi_\nu(z, t) = \epsilon_\nu \phi_\nu(z, t). \tag{3}$$

The single-particle classical motion under H_{sp} is chaotic for large λ, and only becomes regular with some suitable driving parameters and initial conditions. This regular motion can be recognized by the existence of regular resonance islands in the classical phase space that are located around periodic orbits with period sT, where s is an integer [17,23,47]. Quantum mechanically, such regularity of the classical motion corresponds to the existence of s special Floquet states $\phi_\nu(z, t)$, where $\nu = 1, 2, \ldots, s$. Applying a unitary transformation to these Floquet states, one can construct s Wannier-like states that are localized both in space and time and with temporal period sT [47].

In this work, we focus on the $s = 2$ case with $\lambda = 0.12$ and $\omega = 1.4$ as an example [49]. The Floquet states of interest $\phi_1(z, t)$ and $\phi_2(z, t)$ have quasienergies $\epsilon_1 \approx 0.410$ and $\epsilon_2 \approx 1.109$. The two Wannier-like states are related to the two special Floquet states via

$$\Phi_1(z, t) = \frac{1}{\sqrt{2}}[\phi_1(z, t) + e^{-i\pi t/T}\phi_2(z, t)],$$

$$\Phi_2(z, t) = \frac{1}{\sqrt{2}}[\phi_1(z, t) - e^{-i\pi t/T}\phi_2(z, t)], \tag{4}$$

where one can verify that $\Phi_\nu(z, t) = \Phi_\nu(z, t + 2T)$ and $\Phi_1(z, t + T) = \Phi_2(z, t)$. These Floquet states and Wannier-like states have been studied elsewhere [49,50] and are plotted in Fig. 1 of Ref. [50]. The key property we note here is that at $t = 0$, $\Phi_2(z, t = 0)$ is a Gaussian-like wave packet. Therefore, if we prepare a weakly interacting BEC confined in a harmonic trap with suitable initial position $\tilde{h}_0$ above the oscillating mirror and trap frequency $\tilde{\omega}_0$, almost all the atoms will initially occupy the mode $\Phi_2(z, t = 0)$. In our previous TWA calculations in Ref. [50], we chose $\tilde{h}_0 = 9.82$ and $\tilde{\omega}_0 = 0.68$, and found that at $t = 0$, $N_2 \approx 591$ atoms occupy mode $\Phi_2(z, t = 0)$ out of a total atom number $N = 600$. We used over 50 gravitational modes in our TWA treatment, and listed the other parameters in the Table 1 of Ref. [50]. This small difference between N_2 and N is mainly due to the small mismatch between $\Phi_2(z, t = 0)$ and a Gaussian wave packet. We also find that the values of $\tilde{h}_0$ and $\tilde{\omega}_0$ do not need to be fine tuned: A finite perturbation does not significantly reduce N_2 [49].

As pointed out in the Introduction, we have previously studied this system with finite interaction $g \neq 0$ using a multimode phase-space method, namely, the truncated Wigner approximation (TWA) [50]. Interestingly, we find that for $s = 2$ during the whole evolution time $t \leqslant 2000T$ only these two Wannier-like modes are occupied. In Fig. 1(a), we show the total occupation of these two Wannier-like modes $N_s(t) = N_1(t) + N_2(t)$, where $N_i \equiv N_{ii}$ is the occupation number of the mode Φ_i. One can see that the fractional change of $N_s(t)$
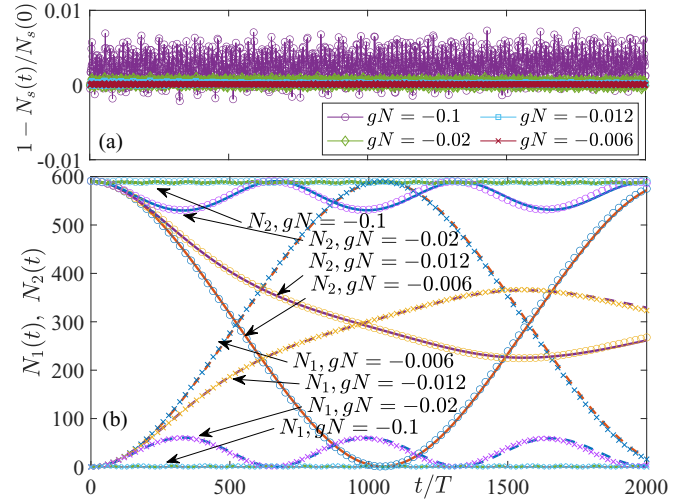

FIG. 1. (a) TWA calculation of the change in number of atoms in the two Wannier-like modes $N_s = N_1 + N_2$ as a function of time. The initial condition is realized by preparing a BEC with $N = 600$ in a harmonic trap at initial height $\tilde{h}_0 = 9.82$ and trap frequency $\tilde{\omega}_0 \approx 0.68$. The change of N_s is less than 1% and remains constant within the fluctuations. (b) Comparison of the occupation numbers N_i of mode Φ_i between the TWA results from Fig. 10 in Ref. [50] and the two-mode results in this work. The solid (dashed) line shows the TWA results for N_2 (N_1), and the circles (crosses) show the two-mode results for N_2 (N_1). The two-mode calculation assumes an initial condition that $N_2 = 591$ atoms occupy mode $\Phi_2(z, 0)$. To compare with the TWA calculation at the critical value $gN = -0.012$, we also need to use a slightly different value $gN = -0.01185$ in the two-mode model for the best comparison.

as a function of time essentially has just small fluctuations around zero. There is also no obvious trend of it increasing during the time window investigated. [In stark contrast, many modes will be occupied if we switch off the driving for the same initial condition and interaction strength (see Ref. [50].] The fluctuations shown in this figure reflect the stochastic nature of the TWA calculations [and imply the actual value of $1 - N_s(t)/N_s(0)$ might be smaller than the calculation uncertainty]. In view of only two modes being important in the TWA calculations for $s = 2$, in this work we apply a so-called two-mode approximation, where we project the Hamiltonian onto the Hilbert subspace spanned by Fock states based on the two modes Φ_1 and Φ_2, which we name the stable-island Hilbert space. We emphasize here that, in contrast to fermionic systems that are limited by the Pauli exclusion principle, our bosonic modes can be occupied by an arbitrary number of atoms. Therefore, the two-mode model is a generic many-body problem for large particle number N, and the stable-island Hilbert space has a dimension of $N + 1$.

While the two-mode model is described in detail in the next sections, here in Fig. 1(b), we first show the excellent agreement of the TWA and the two-mode results for different interaction strengths gN. We emphasize that our TWA calculations [50] show that a DTC forms for interaction strengths above $g_c N = -0.012$ for an initial state prepared in a harmonic trap with initial position $\tilde{h}_0$ and trap frequency $\tilde{\omega}_0$. Quantum fluctuations become significant near this critical in-

teraction strength $g_c N$, and the TWA deviates strongly from the mean-field results. Nevertheless, the two-mode model is still in excellent agreement with the TWA in this case. The TWA can in principle include effects of many (much more than two) modes, and describe the many-body quantum dynamics exactly in the asymptotic $N \to \infty$ limit. On the other hand, although the two-mode model only includes two modes, it can describe the quantum evolution within the truncated stable-island Hilbert space exactly for any arbitrary N. The excellent agreement between these two models gives us confidence that leakage of atoms to modes other than Φ_1 and Φ_2 is negligible during $t \leqslant 2000T$ and most of the atoms seem to be able to remain in the stable-island Hilbert space for a much longer time. The fact that most atoms are "trapped" in this stable-island Hilbert space for a long time breaks the ergodicity of the system and prevents Floquet heating. The underlying physics may be related to a quantum version of the Kolmogorov-Arnold-Moser (KAM) theory as pointed out in Ref. [27], where the existence of a stable island (as tori in phase space) is robust against weak interactions [53]. However, nonergodicity in KAM theory can be destroyed by an Arnold diffusion after an astronomically long time [27], implying DTC in our system has a finite lifetime.

III. TWO-MODE APPROXIMATION

In the two-mode approximation, we assume the bosonic atom field operator can be expanded solely in terms of the two Wannier-like modes

$$\hat{\Psi}(z) = \sum_{i=1,2} \hat{a}_i(t)\Phi_i(z,t), \quad \hat{\Psi}^\dagger(z) = \sum_{i=1,2} \hat{a}_i^\dagger(t)\Phi_i^*(z,t), \quad (5)$$

where $\hat{a}_i(t)$ and $\hat{a}_i^\dagger(t)$ are the annihilation and creation operators of a boson in the time-dependent mode $\Phi_i(z,t)$. The time dependence of the creation operators obeys $a_i^\dagger(t) = a_i^\dagger(t + 2T)$ and $a_1^\dagger(t + T) = a_2^\dagger(t)$, which are determined by the properties of $\Phi_i(z,t)$, and similar rules apply to the annihilation operators. One can obtain a many-body basis set via the Fock state [54]

$$|n_1, n_2; t\rangle = \frac{[\hat{a}_1^\dagger(t)]^{n_1}}{\sqrt{n_1!}} \frac{[\hat{a}_2^\dagger(t)]^{n_2}}{\sqrt{n_2!}} |0, 0\rangle, \quad (6)$$

where n_1 is the number of atoms in mode Φ_1 and n_2 is the number of atoms in mode Φ_2. Expanding the many-body state vector in this basis set gives

$$|\Theta(t)\rangle = \exp(-i\mu t) \sum_{n=0}^{N} b_n(t)|n, N - n; t\rangle, \quad (7)$$

where the total number of bosonic atoms N is a good quantum number and μ is a suitable frequency (chosen below). These Fock states also satisfy $|n_1, n_2; t + 2T\rangle = |n_1, n_2; t\rangle$ and $|n_1, n_2; t + T\rangle = |n_2, n_1; t\rangle$. We note that, while both the creation and annihilation operators and the Fock-state basis are time dependent, the matrix elements of any direct product of creation and annihilation operators at the same time are time independent, e.g., $\langle n_1 + 1, n_2 - 1; t|\hat{a}_1^\dagger(t)\hat{a}_2(t)|n_1, n_2; t\rangle = \sqrt{(n_1 + 1)n_2}$.

The time evolution of the expansion coefficients $b_n(t)$ is determined by the many-body Schrödinger equation, in a vector form

$$[\underline{\widetilde{H}}(t) - i\hbar\partial_t]\vec{b}(t) = 0, \quad (8)$$

where $\underline{\widetilde{H}}(t)$ is a time-dependent matrix with matrix elements $\widetilde{H}_{mn}(t) = \langle m, N - m; t|\hat{\mathcal{H}}(t)|n, N - n; t\rangle$. Here, the effective Hamiltonian operator is given by

$$\hat{\mathcal{H}}(t) = J(\hat{a}_1^\dagger\hat{a}_2 + \text{H.c.}) + \frac{1}{2}g\sum_{ijkl=1}^{2} U_{ijkl}(t)\hat{a}_i^\dagger\hat{a}_j^\dagger\hat{a}_k\hat{a}_l, \quad (9)$$

where $J = (\epsilon_1 - \epsilon_2 + \hbar\omega/2)/2$ and $U_{ijkl}(t) = \int dz\, \Phi_i^*(z,t)\Phi_j^*(z,t)\Phi_k(z,t)\Phi_l(z,t)$. The phase factor μ occurring in the quantum state $|\Theta(t)\rangle$ is given by $\mu = N\epsilon/\hbar$, where $\epsilon = (\epsilon_1 + \epsilon_2 - \hbar\omega/2)/2$. The derivation is given in Appendix A 1. With an understanding that the creation and annihilation operators will always act on the Fock basis and introducing time-independent matrix elements, we hereafter leave implicit the time dependence of $\hat{a}_i$ and $\hat{a}_i^\dagger$. The only explicit time dependence remains in the parameter $U_{ijkl}(t)$, which is periodic with period $\widetilde{T} = 2T$ and $\widetilde{\omega} = \omega/2$. The effective Hamiltonian matrix $\underline{\widetilde{H}}(t)$ also shares the same periodicity, implying that Eq. (8) can be formally solved using a Floquet approach. A many-body Floquet state and Floquet energy can be defined as

$$[\underline{\widetilde{H}}(t) - i\hbar\partial_t]\vec{\mathcal{F}}_\nu(t) = \tilde{\mathcal{E}}_\nu\vec{\mathcal{F}}_\nu(t), \quad (10)$$

and the time evolution can be obtained via $\vec{b}(t) = \sum_\nu \mathcal{C}_\nu\vec{\mathcal{F}}_\nu(t)e^{-i\tilde{\mathcal{E}}_\nu t}$ and $\mathcal{C}_\nu = \vec{\mathcal{F}}_\nu^\dagger(t = 0)\vec{b}(0)$ (see Appendix B). We emphasize here that this approach, namely, the many-body Floquet (MBF) approach, is a full and exact many-body quantum calculation as long as only two modes are occupied and depletion to other modes is negligible.

Another timescale in the Hamiltonian is given by $t_{\text{tunneling}} = 1/J$ which describes the tunneling of a single particle between the two modes. $t_{\text{tunneling}}$ typically is on the order of $500T$, much longer than $2T$, the period of $U_{ijkl}(t)$. An approximation to simplify and understand this problem is therefore to take a high-frequency expansion (HFE) of the Hamiltonian matrix $\underline{\widetilde{H}}(t) = \sum_\delta \underline{h}_\delta e^{-i\delta\tilde{\omega}t}$, where $\underline{h}_\delta = \int_0^{\widetilde{T}} dt\, \underline{\widetilde{H}}(t)e^{i\delta\tilde{\omega}t}/\widetilde{T}$, and keep only the lowest order $\underline{h}_0$, which is a time-independent effective Hamiltonian matrix. The corresponding Hamiltonian operator $\hat{h}_0$ of $\underline{h}_0$ agrees with the one given in Ref. [4], which can be expressed in the same form as Eq. (9) with $U_{ijkl}(t)$ replaced by the $2T$-average value $\bar{U}_{ijkl} = \int_0^{2T} U_{ijkl}(t)dt/2T$. However, we note that the time-independent Hamiltonian in Ref. [4] is derived by expanding and truncating the Floquet Hamiltonian and field operators in an extended space-time Hilbert space. This expansion and truncation is thus an approximation that is effectively equivalent to our HFE approximation. Under the HFE approximation, the time evolution can be approximately given by $\vec{b}(t) = \sum_\nu c_\nu\vec{f}_\nu e^{-i\mathcal{E}_\nu t}$ and the initial condition $c_\nu = \vec{f}_\nu^\dagger\vec{b}(0)$. Here, $\mathcal{E}_\nu$ and $\vec{f}_\nu$ are eigenenergies and eigenstates of $\underline{h}_0$: $\underline{h}_0\vec{f}_\nu = \mathcal{E}_\nu\vec{f}_\nu$.

Discussions on SDTTSB usually refer to initial states without extensive many-body quantum entanglement, which are
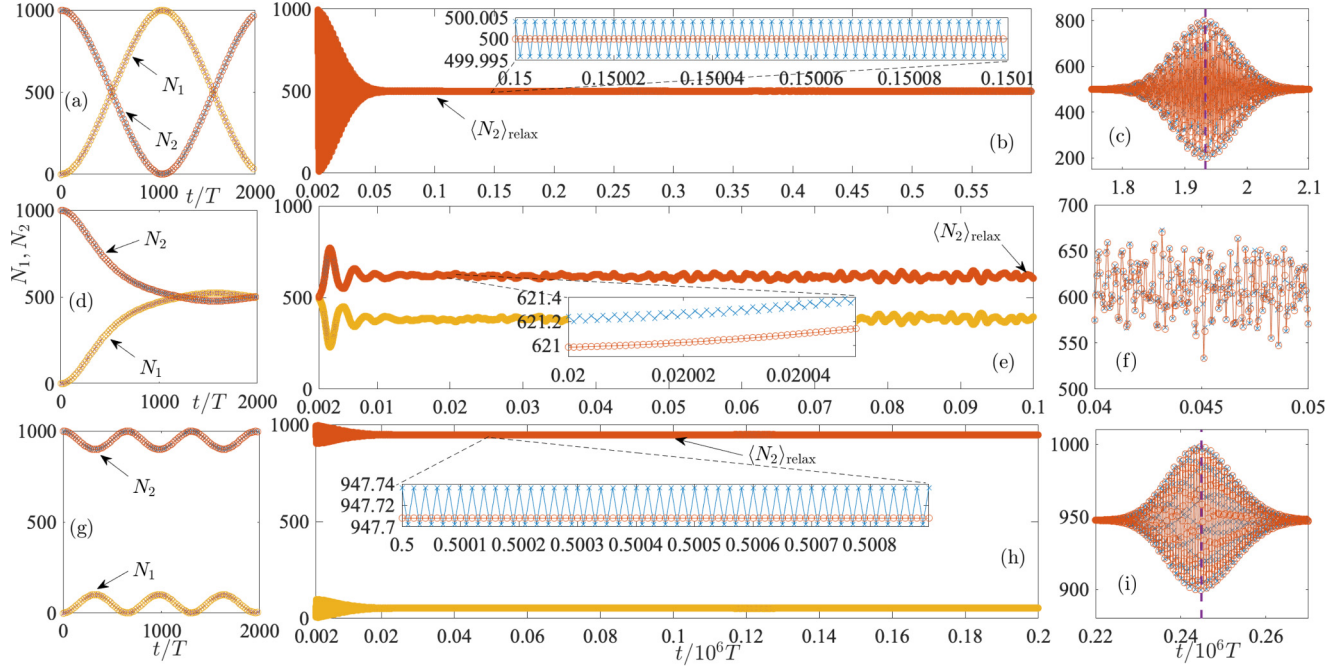
FIG. 2. N_1 and N_2 as a function of time for (a)–(c) weak interaction $gN = -0.006$, (d)–(f) near-critical interaction $gN = -0.012$, and (g)–(i) strong interaction $gN = -0.02$, for the initial state $|0, N\rangle$ with total particle number $N = 1000$. The crosses (circles) show results from the MBF approach (HFE approximation). (a), (d), (g) show the short-time behavior (at $t = 0, 20, \ldots, 2000T$ for better resolution), where the HFE approximation works perfectly. (b), (e), (h) show the behavior on a much longer timescale, where N_2 relaxes to some steady value $\langle N_2 \rangle_{\text{relax}}$. For small interaction $gN = -0.006$, $\langle N_2 \rangle_{\text{relax}} = N/2$. At interaction $gN = -0.012$ near the critical value, stronger fluctuations occur around the relaxation. At strong interaction $gN = -0.02$, $\langle N_2 \rangle_{\text{relax}} > N/2$ without fluctuations. Zoom-ins shown in the insets of (b), (e), and (h) illustrate minor differences between the MBF and HFE approximation. (c), (f), (i) At very long times, a strong quantum revival at around t_{revival} (see Fig. 9) appears for both strong and weak interactions, but not for interactions near the critical value. Only data for every $100T$ are shown for clarity.

physically accessible by simple preparation schemes. As mentioned before, by preparing a BEC in a harmonic trap with suitable potential height and width, the initial condition can be well approximated by a product state $|0, N\rangle$. If we turn off the interaction in the preparation stage, the particles can tunnel from Φ_2 to Φ_1 with a tunneling rate J, and an additional relative phase can also be induced by some phase-printing scheme. Therefore, in principle, we can prepare a BEC initial product state, which in first quantization is

$$|\{\theta, \varphi\}\rangle = |\Lambda_2\rangle_1 |\Lambda_2\rangle_2 \ldots |\Lambda_2\rangle_N, \tag{11}$$

where all atoms occupy a single mode $\Lambda_2 = \sin\theta e^{i\varphi} \Phi_1 + \cos\theta \Phi_2$. Without loss of generality, we choose $\theta \in [0, \pi)$ and $\varphi \in [0, \pi)$.

To investigate the dynamical evolution, we study the observables $N_{ij}(t) = \langle \Theta(t) | \hat{a}_i^\dagger \hat{a}_j | \Theta(t) \rangle$, which play a similar role to the one-body reduced density matrix elements. For simplification of notation, we define $N_i(t) \equiv N_{ii}(t)$. Figure 2 shows a comparison between the MBF approach and HFE approximation for $gN = -0.006$, -0.012, and -0.02. The initial state is chosen as $|0, N\rangle$ with $N = 1000$. Figures 2(a), 2(d), and 2(g) show perfect agreement between the HFE and MBF at relatively short timescales (0 to $2000T$). At longer timescales $t > t_{\text{relax}}$, Figs. 2(b), 2(e), and 2(h) show that $N_2(t)$ relaxes to a constant $\langle N_2 \rangle_{\text{relax}}$ for the HFE. However, for an interaction strength near the critical value $gN = -0.012$, $N_2(t)$ has a relatively larger fluctuation. The MBF results here also

show excellent agreement with the HFE, except for an almost negligible oscillation around the $\langle N_2 \rangle_{\text{relax}}$ that can only be seen in the insets for a large zoom-in scale. This small oscillation can be understood as micromotion originating from the time dependence of the many-body Floquet states in the MBF approach. After an even longer evolution time, Figs. 2(c) and 2(i) show a strong quantum revival for both strong and weak interaction, but no revival can be seen for the critical case, Fig. 2(f). We also note that for $gN = -0.02$, the quantum revival seems to be almost perfect, i.e., $N_2(t_{\text{revival}}) \approx N$, in contrast to the case for $gN = -0.006$ where $N_2(t_{\text{revival}}) < N$. Visible differences between the MBF and HFE show up in the quantum revival regime. Nevertheless, the HFE still accurately predicts the revival time t_{revival} and the overall revival profile. As one can see, the HFE is an excellent approximation. The HFE will also provide insight into the symmetry breaking and give an analytical explanation of the time-evolution behavior, as shown in the next section.

While the quantum revival is interesting and indicates there is a relatively short transient period of deviation from an almost perfect temporal periodicity, the revival regime is much shorter than the steady-state regime. We discuss the quantum revivals with more detail in Appendix C and focus on the steady-state regime here. We emphasize that this relaxation value of $\langle N_2 \rangle_{\text{relax}}$ reflects the time-translational symmetry of the steady state. For example, the quantum correlation function (QCF) $P(z, z^\#, t) = \text{Tr}[\hat{\Psi}^\dagger(z^\#)\hat{\Psi}(z)|\Theta(t)\rangle\langle\Theta(t)|]$

is given by

$$P(z, z^{\#}, t) = \sum_{i,j=1}^{2} N_{ji}(t)\Phi_i(z, t)\Phi_j^*(z^{\#}, t), \quad (12)$$

where z and $z^{\#}$ refer to two different position coordinates. The position probability density at stroboscopic times $t = kT$ with $k = 1, 2, 3, \ldots$ can be well approximated by $F(z, kT) = P(z, z, kT) \approx N_1(kT)|\Phi_1(z, kT)|^2 + N_2(kT)|\Phi_2(z, kT)|^2$, where the cross terms can be neglected since Φ_1 and Φ_2 are well-separated localized wave packets at $t = kT$. We recall that $\Phi_1(z, kT) = \Phi_2(z, kT + T)$. Therefore, if $\langle N_2(t) \rangle \to \langle N_2 \rangle_{\text{relax}} = N/2$ as in Fig. 2(b), $F(z, kT) = F(z, kT + T)$ has the same period as the Hamiltonian, which represents a symmetry-unbroken state. On the other hand, if $\langle N_2(t) \rangle \to \langle N_2 \rangle_{\text{relax}} \neq N/2$ as in Fig. 2(h), $F(z, kT) \neq F(z, kT + T)$ and $F(z, kT) = F(z, kT + 2T)$, indicating that the system's state breaks the discrete time-translational symmetry, i.e., a time crystal is present. Figures 2(h) and 2(i) predict that the time crystal survives for times out to at least 250 000 driving periods.

We can also define a one-body projection operator (OBP) $\hat{M}_G$ onto the Gaussian-like localized wave packet $\Phi_2(z, 0)$ as an observable [50]. In the first quantization, the OBP is given by $\hat{M}_G = \sum_{i=1}^{N} (|\chi\rangle\langle\chi|)_i$, where $\langle z|\chi\rangle = \Phi_2(z, 0)$ and i lists individual particles as $i = 1, 2, \ldots, N$. The expectation value of the OBP can be related to the QCF $\langle \hat{\Psi}(z^{\#})^{\dagger}\hat{\Psi}(z) \rangle$ via $M_G(t) = \iint dz\, dz^{\#} \Phi_2(z^{\#}, 0)\langle \hat{\Psi}(z^{\#})^{\dagger}\hat{\Psi}(z) \rangle \Phi_2^*(z, 0)$. At stroboscopic times $t = kT$, the OBP can be simplified as

$$M_G(kT) = \begin{cases} N_1(kT) = N - N_2(kT), & k = 1, 3, 5, \ldots \\ N_2(kT), & k = 0, 2, 4, \ldots \end{cases} \quad (13)$$

The physical picture is clear: $M_G(kT)$ measures how many atoms occupy the Gaussian-like wave packet $\Phi_2(z, 0)$ at stroboscopic times. When k is even (odd), this Gaussian-like wave packet coincides with $\Phi_2(z, kT)$ [$\Phi_1(z, kT)$]. Therefore, via the investigation of the behavior of $N_2(kT)$, we can obtain the evolution of the observable $M_G(kT)$, which reveals the temporal symmetry of the steady state. If $\langle N_2 \rangle_{\text{relax}} = N/2$, then $M_G(kT) \to N/2$ implies a T periodicity. On the contrary, if $\langle N_2 \rangle_{\text{relax}} \neq N/2$, $M_G(kT)$ has $2T$ periodicity, indicating SDTTSB. One can define a frequency response observable via the Fourier transformation

$$m_G(f) = \frac{1}{K}\sum_{k=k_0}^{k_0+K-1} e^{-ifkT}\frac{M_G(kT)}{N}, \quad (14)$$

where we usually choose $K = 2048$ and $k_0 = 10^4$ so that k_0T is in the steady-state regime. In particular, the subharmonic response is given by

$$|m_G(\omega/2)| \to \frac{|N - 2\langle N_2 \rangle_{\text{relax}}|}{2N} = \frac{P_G}{2}, \quad (15)$$

where $P_G = |\langle N_2 \rangle_{\text{relax}} - \langle N_1 \rangle_{\text{relax}}|/N$ is the population imbalance. $|m_G(\omega/2)| = 0$ (or equivalently $P_G = 0$) indicates the symmetry-unbroken phase, and hence $|m_G(\omega/2)|$ can be regarded as an order parameter.

IV. SYMMETRY BREAKING

Under the HFE approximation, the effective time-independent Hamiltonian satisfies the $\mathbb{Z}_2$ symmetry determined by the operator $\hat{P}_{12} = i^N \exp[i\pi(\hat{a}_1^{\dagger}\hat{a}_2 + \hat{a}_2^{\dagger}\hat{a}_1)/2]$ which interchanges the mode indices $1 \leftrightarrow 2$. We find that $\hat{P}_{12}\hat{a}_1\hat{P}_{12}^{-1} = i\hat{a}_2$ and $\hat{P}_{12}\hat{a}_2\hat{P}_{12}^{-1} = i\hat{a}_1$. The corresponding effective Hamiltonian operator can be rewritten as

$$\hat{h}_0 = J(\hat{a}_1^{\dagger}\hat{a}_2 + \text{H.c.}) + gu_T(\hat{a}_1^{\dagger}\hat{N}\hat{a}_2 + \text{H.c.})$$
$$+ \frac{1}{2}g\left[u_I\sum_{i=1}^{2}\hat{N}_i(\hat{N}_i - 1) + 4u_N\hat{N}_1\hat{N}_2\right]$$
$$+ \frac{1}{2}gu_P(\hat{a}_1^{\dagger}\hat{a}_1^{\dagger}\hat{a}_2\hat{a}_2 + \text{H.c.}), \quad (16)$$

where $u_T = \bar{U}_{1112}$, $u_I = \bar{U}_{1111}$, $u_N = \bar{U}_{1212}$, and $u_P = \bar{U}_{1122}$ are the only four distinctive values of $\bar{U}_{ijkl}$ constrained by the $\mathbb{Z}_2$ symmetry (see Appendix A 2). The effective Hamiltonian $\hat{h}_0$ is invariant under the symmetry operator $\hat{P}_{12}$. Here, the number operators are given by $\hat{N}_1 = \hat{a}_1^{\dagger}\hat{a}_1$, $\hat{N}_2 = \hat{a}_2^{\dagger}\hat{a}_2$, and $\hat{N} = \hat{N}_1 + \hat{N}_2$. One might notice, under a mean-field approximation, that this effective Hamiltonian can be applied to investigate the bosonic self-trapping phenomenon, for example, in a BEC in a double-well potential [51]. The connection of DTC formation and self-trapping was recognized in Ref. [4]. Here, we go beyond the mean-field approximation, and numerically investigate the whole eigenspectrum exactly. In our numerical investigation here, we have $J \approx 3.580 \times 10^{-4}$, $u_I \approx 0.2237$, $u_N \approx 0.0519$, $u_T \approx -1.9 \times 10^{-4}$, and $u_P \approx -4.3 \times 10^{-6}$. Since the spectrum of $\hat{h}_0$ is bounded from both below and above, the maximum and minimum eigenenergy of the $\hat{h}_0$ can be obtained via the mean-field approach in the large-N limit. Neglecting the term associated with u_P (which is much smaller than u_T, u_I, and u_N), this approach leads to

$$E_{\text{max}} \approx E_{\text{shift}} + |\tilde{J}|N/2 \quad (17)$$

and

$$E_{\text{min}} \approx \begin{cases} E_{\text{shift}} - |\tilde{J}|N/2, & |gN| \leqslant |g_bN| \\ \frac{1}{2}gN^2u_I + \frac{\tilde{J}^2N}{gN(u_I - 2u_N)}, & |gN| > |g_bN| \end{cases} \quad (18)$$

where $g_bN \equiv -2J/(u_I - 2u_N + 2u_T)$. (We use the conditions $J > 0$ and $gN < 0$ here. We also focus on the case $J + gNu_T > 0$ since $|gN|$ is small. See Appendix D for details.) Here, $E_{\text{shift}} = gN(u_IN/2 - u_I + u_NN)/2$ and its physical meaning will be clear below.

For a given total number N (since $\hat{N}$ commutes with $\hat{h}_0$), the Hamiltonian can be mapped to the Lipkin-Meshkov-Glick (LMG) model (see Appendix A 3) as [49,55,56]

$$\hat{h}_0 \approx \tilde{J}\left(-\hat{S}_x + \frac{\gamma}{N}\hat{S}_z^2\right) + E_{\text{shift}}, \quad (19)$$

with $\hat{S}_x = (\hat{a}_1^{\dagger}\hat{a}_2 + \hat{a}_2^{\dagger}\hat{a}_1)/2$ and $\hat{S}_z = (\hat{a}_2^{\dagger}\hat{a}_2 - \hat{a}_1^{\dagger}\hat{a}_1)/2$, which are bosonic spin operators. The LMG Hamiltonian can be applied to describe spin systems with infinite-range interaction. However, we emphasize here that our system consists of bosonic atoms with zero-range contact interactions. When the two-mode and HFE approximations are applicable, the time-independent LMG Hamiltonian in Eq. (19) becomes an
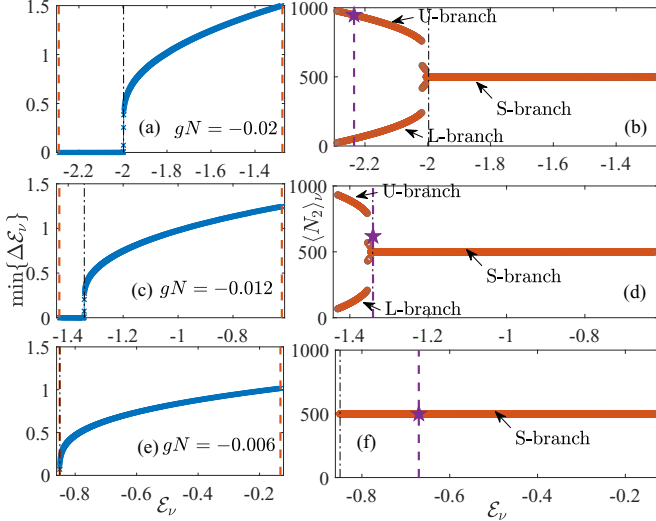
FIG. 3. Symmetry-breaking edge of the two-mode Hamiltonian with $N = 1000$ as a function of eigenenergy $\mathcal{E}_\nu$. (a), (c), (e) show the minimum of the gap $\min\{\Delta\mathcal{E}_\nu\}$ between adjacent eigenenergies for $gN = -0.02$, -0.012, and -0.006, respectively. The symmetry-breaking edge indicated by the black dashed-dotted vertical line and the range of eigenenergies are given by $E_{\min}$ and $E_{\max}$ indicated by the red dashed vertical lines on the left and right. $\min\{\Delta\mathcal{E}_\nu\}$ is essentially zero for a near-degenerate pair as shown in (a) and (c) for eigenenergies below the edge. In (e), the edge is about the same as the minimum of the spectrum $E_{\min}$ and hence no near-degenerate pair exists. (b), (d), (f) show $\langle N_2\rangle_\nu$ in Eq. (21) as a function of $\mathcal{E}_\nu$, where the onset of bifurcation occurs at the edge indicated by the black vertical dashed-dotted line. We name the eigenstates with no bifurcation of $\langle N_2\rangle_\nu = N/2$ the S branch and $\langle N_2\rangle_\nu > N/2$ ($\langle N_2\rangle_\nu < N/2$) in the bifurcation regime the U branch (L branch). The purple dashed line shows the initial energy E_{ini} for the initial state $|0, N\rangle$, and the purple pentagram shows the corresponding relaxation value $\langle N_2\rangle_{\text{relax}}$.

excellent approximation for the Floquet Hamiltonian of the underlying physical system, and determines the dynamical properties of the original system. The LMG Hamiltonian is invariant under the symmetry operator $\hat{P}_{12}$. The parameters are given by $\tilde{J} = -2[J + gu_T(N - 1)]$, $\gamma = gN(u_I - 2u_N)/\tilde{J}$. In the case of large N and finite $\gamma \propto gN$, a symmetry-broken edge exists for the LMG Hamiltonian [17,49,55,56]:

$$\mathcal{E}_{\text{edge}} \approx -|\tilde{J}|N/2 + E_{\text{shift}}. \quad (20)$$

For $\mathcal{E}_\nu > \mathcal{E}_{\text{edge}}$ the eigenenergies are nondegenerate while those for $\mathcal{E}_\nu < \mathcal{E}_{\text{edge}}$ are essentially twofold degenerate (see Fig. 3). From the expression for $E_{\min}$ and $\mathcal{E}_{\text{edge}}$, one can observe that $E_{\min} = \mathcal{E}_{\text{edge}}$ for weak interaction $|gN| < |g_bN|$, where g_bN is defined above and Eq. (D9). For strong interaction $|gN| > |g_bN|$, $E_{\min} < \mathcal{E}_{\text{edge}} < E_{\max}$ and the eigenpairs below and above the edge have distinct features. We emphasize that, according to group representation theory, since $\mathbb{Z}_2$ is the symmetry group, the eigenstates for $\hat{h}_0$ would in general be nondegenerate and either even or odd under the symmetry operator, i.e., $\hat{P}_{12}|\nu, \pm\rangle = \pm|\nu, \pm\rangle$. However, for $|gN| > |g_bN|$, eigenstates that satisfy $\mathcal{E}_\nu < \mathcal{E}_{\text{edge}}$ form near-degenerate pairs $|\nu, +\rangle$ and $|\nu, -\rangle$ of opposite symmetry, with an energy gap $|\mathcal{E}_\nu^{(+)} - \mathcal{E}_\nu^{(-)}|$ that is exponentially small in N. This energy gap is negligible for a large
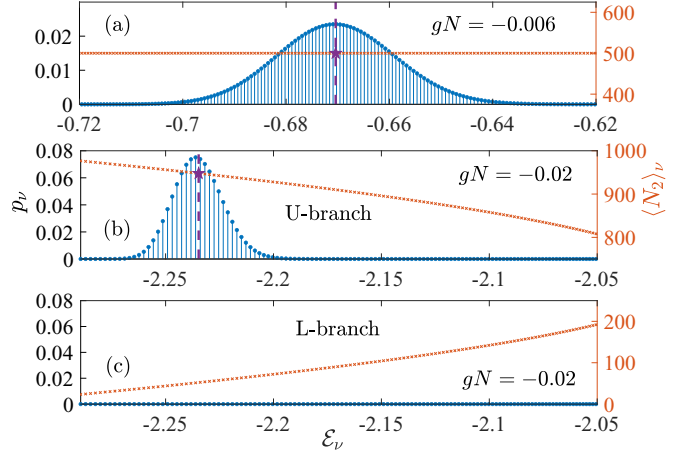

FIG. 4. Projection $p_\nu = |c_\nu|^2$ of initial state $|0, N\rangle$ with $N = 1000$ as a function of $\mathcal{E}_\nu$ (blue circles) and the corresponding $\langle N_2\rangle_\nu$ (red crosses). (a) shows the projection for the case $gN = -0.006$, which is only significant around the initial energy E_{ini} indicated by the purple dashed vertical line. The diagonal ensemble prediction $\sum_\nu p_\nu\langle N_2\rangle_\nu = N/2$ is indicated by the purple pentagram. (b), (c) show the projection to the U and L branch, respectively, for $gN = -0.02$. The projection is only significant for the U branch around the initial energy E_{ini}. The diagonal ensemble prediction is indicated by the purple pentagram.

and finite N in practice, and becomes exactly zero in the infinite-N (thermodynamic) limit. Therefore, we can choose a pair of symmetry-broken states that satisfy $\hat{P}_{12}|\nu\rangle_U = |\nu\rangle_L$ and $\hat{P}_{12}|\nu\rangle_L = |\nu\rangle_U$, which are given by $|\nu\rangle_U = (|\nu, +\rangle + |\nu, -\rangle)/\sqrt{2}$ and $|\nu\rangle_L = (|\nu, +\rangle - |\nu, -\rangle)/\sqrt{2}$. $|\nu\rangle_U$ and $|\nu\rangle_L$ have the same expectation energies $\mathcal{E}_\nu^{(U)} = \mathcal{E}_\nu^{(L)}$ and serve as a degenerate pair of symmetry-broken eigenstates. In contrast, any eigenstates with eigenenergies $\mathcal{E}_\nu > \mathcal{E}_{\text{edge}}$ show no near degeneracy and these states $|\nu\rangle_S$ are symmetry unbroken. Figures 3(a), 3(c), and 3(e) show the symmetry-breaking edge for $gN = -0.02$, -0.012, and -0.006, respectively. The vertical axis shows the minimum of adjacent gaps: $\min\{\Delta\mathcal{E}_\nu\} = \min(\mathcal{E}_\nu - \mathcal{E}_{\nu-1}, \mathcal{E}_{\nu+1} - \mathcal{E}_\nu)$, which is exactly zero if and only if there is a double degeneracy. One can see that this quantity indeed becomes essentially zero at $\mathcal{E}_{\text{edge}}$, which is denoted by the black vertical dashed-dotted lines. The red dashed line on the right (left) indicates $\mathcal{E}_{\min}$ ($\mathcal{E}_{\max}$). For $|gN| \leqslant |g_bN| \approx 0.006$, only a symmetry-unbroken phase exists since $\mathcal{E}_{\text{edge}} \approx \mathcal{E}_{\min}$, and no near-degenerate pairs of energy levels occur.

A particularly useful observable to illustrate the importance of the symmetry-breaking edge is $\langle N_2\rangle_\nu$ and $\langle N_1\rangle_\nu = N - \langle N_2\rangle_\nu$, where $\langle O\rangle_\nu \equiv \langle\nu|\hat{O}|\nu\rangle$ and

$$\langle N_2\rangle_\nu = \begin{cases} \langle N_2\rangle_\nu^{(U)} \text{ or } \langle N_2\rangle_\nu^{(L)}, & \mathcal{E}_\nu < \mathcal{E}_{\text{edge}} \\ \langle N_2\rangle_\nu^{(S)}, & \mathcal{E}_\nu \geqslant \mathcal{E}_{\text{edge}}. \end{cases} \quad (21)$$

For symmetry-unbroken states, the permutation symmetry between modes ensures that $\langle N_1\rangle_\nu^{(S)} = \langle N_2\rangle_\nu^{(S)} = N/2$. On the other hand, for symmetry-broken states, we have $\langle N_1\rangle_\nu^{(U)} = \langle N_2\rangle_\nu^{(L)}$ and $\langle N_1\rangle_\nu^{(L)} = \langle N_2\rangle_\nu^{(U)}$, but in general $\langle N_2\rangle_\nu^{(U)} \neq \langle N_2\rangle_\nu^{(L)} \neq N/2$. Without loss of generality, we denote $\langle N_2\rangle_\nu^{(U)} > \langle N_2\rangle_\nu^{(L)}$ (hence the U and L branches). Figures 3(b), 3(d), and 3(f) show $\langle N_2\rangle_\nu$ as a function of $\mathcal{E}_\nu$, with initial state $|0, N\rangle$ and $N = 1000$. The black dashed-dotted

vertical line indicates the symmetry-broken edge, which illustrates the onset of bifurcation of $\langle N_2 \rangle_\nu$ as a function of $\mathcal{E}_\nu$. We also show $\langle N_2 \rangle_{\text{relax}}$ by the purple pentagram symbol and the initial energy $E_{\text{ini}} = \langle \Theta(0) | \hat{h}_0 | \Theta(0) \rangle$ by the dashed vertical line. Numerically, $\langle N_2 \rangle_{\text{relax}}$ is calculated by averaging $\langle N_2 \rangle_{\text{relax}} = \sum_{k=k_0}^{k_0+K-1} \langle N_2(kT) \rangle / K$ over a time window of $K = 2048$ driving periods at $k_0 T = 10^4 T$. We can see that the relaxation value lies on the $\langle N_2 \rangle_\nu - \mathcal{E}_\nu$ curve of the corresponding branches, which can be understood via dephasing. In general, for an initial state $|\Theta(0)\rangle = \sum_\nu c_\nu |\nu\rangle$, the time evolution of an observable is given by $\langle O \rangle(t) = \sum_{\mu\nu} c_\mu^* c_\nu \langle \nu | O | \mu \rangle e^{-i(\mathcal{E}_\nu - \mathcal{E}_\mu)t}$. Typically, c_ν only has noticeable values around a small energy window close to the initial energy. If there is no degeneracy, after long enough time, dephasing leads to $\langle O \rangle_{\text{relax}} = \sum_\nu p_\nu \langle O \rangle_\nu = \text{Tr}[\rho_d \hat{O}]$, where $\rho_d = \sum_\nu p_\nu |\nu\rangle\langle\nu|$ is sometimes called the diagonal ensemble, and $p_\nu = |c_\nu|^2$ is the projection probability of the initial state to the ν's eigenstate. Essentially, the contributions for $\mu \neq \nu$ cancel out for large t, as the phase factors in $\langle O \rangle(t)$ become more random. The initial energy can also be given by the diagonal ensemble $E_{\text{ini}} = \sum_\nu p_\nu \mathcal{E}_\nu = \text{Tr}[\rho_d \hat{h}_0]$. When the initial energy is well above the broken edge, $\langle N_2 \rangle_\nu = N/2$ gives $\langle N_2 \rangle_{\text{relax}} = N/2$ as shown in Fig. 4(a). When the initial energy is below the broken edge, as shown in Figs. 4(b) and 4(c), we find that for initial state $|0, N\rangle$, only the U branch has noticeable projections since the degeneracy is lifted in a single branch, the dephasing formula still works, and gives $\langle N_2 \rangle_{\text{relax}} = \sum_\nu p_\nu \langle N_2 \rangle_\nu$.

To further explore the corresponding relation between the initial energy and the relaxation value, we investigate the case with an initial state $|\Theta(0)\rangle = |\{\theta, \varphi\}\rangle$ defined in Eq. (11) with all bosons in a mode given by $\Lambda_2 = \sin\theta e^{i\varphi}\Phi_1 + \cos\theta\Phi_2$, which has initial energy $E_{\text{ini}}(\theta, \varphi) = \langle\{\theta, \varphi\}|\hat{h}_0|\{\theta, \varphi\}\rangle$. Since this initial state represents all atoms occupying the same single-particle state, the initial energy reduces to a mean-field expression

$$\frac{E_{\text{ini}}(\theta, \varphi)}{N} \approx J \sin 2\theta \cos(\varphi) + gN\left[\frac{u_I}{2} + u_T \sin 2\theta \cos(\varphi)\right.$$
$$\left. + \frac{(2u_N - u_I)}{4} \sin^2 2\theta\right]. \quad (22)$$

Figure 5 shows $\langle N_2 \rangle_{\text{relax}}$ as a function of the initial energy $E_{\text{ini}}(\theta, \varphi = 0)$ for different initial states $|\{\theta, \varphi = 0\}\rangle$, and $\langle N_2 \rangle_\nu$ as a function of $\mathcal{E}_\nu$ for $gN = -0.1$. As one can see, in the deep regime in all branches (L, U, and S), these two curves overlap, implying the dephasing mechanism leads to relaxation except very close to the critical point where finite-size effects become important. The inset shows the corresponding relationship between the initial state θ and the initial energy $E_{\text{ini}}(\theta, \varphi = 0)$. We also note that the initial states considered here are initial states with no multimode entanglement, as these are the initial states of interest for spontaneous symmetry-breaking physics.

In Fig. 6(a), we investigate the subharmonic response $|m_G(\omega/2)|$ of the steady state as a function of $|gN|$ for different initial states $|\Theta(0)\rangle = |\{\theta, \varphi = 0\}\rangle$, which changes from 0 to a finite value abruptly around a critical $|g_c N|$ indicated by the thin vertical lines. These critical values for different θ can be obtained by equating $E_{\text{ini}}(\theta, \varphi = 0)$ and $\mathcal{E}_{\text{edge}}$ as
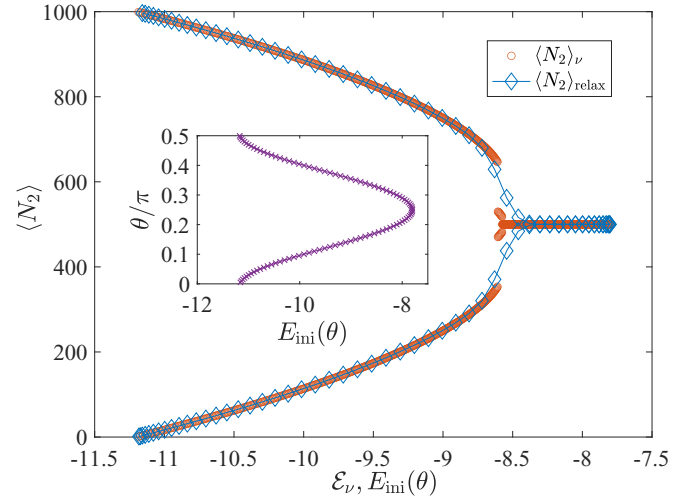

FIG. 5. $\langle N_2 \rangle_{\text{relax}}$ (blue diamonds) for different initial states as a function of the initial energy $E_{\text{ini}}(\theta) \equiv E_{\text{ini}}(\theta, \varphi = 0)$ in Eq. (22) for $gN = -0.1$. Except in the vicinity of the symmetry-breaking edge, the curve of $\langle N_2 \rangle_\nu$ versus $\mathcal{E}_\nu$ (red circles) overlaps with the curve of $\langle N_2 \rangle_{\text{relax}}$ versus $E_{\text{ini}}(\theta)$, which implies dephasing is the underlying mechanism for the relaxation process as described in Fig. 4. The inset shows the relationship between the initial state θ and the initial energy E_{ini}. We choose to present the result for $0 \leqslant \theta \leqslant \pi/2$ out of the full range between 0 and π.
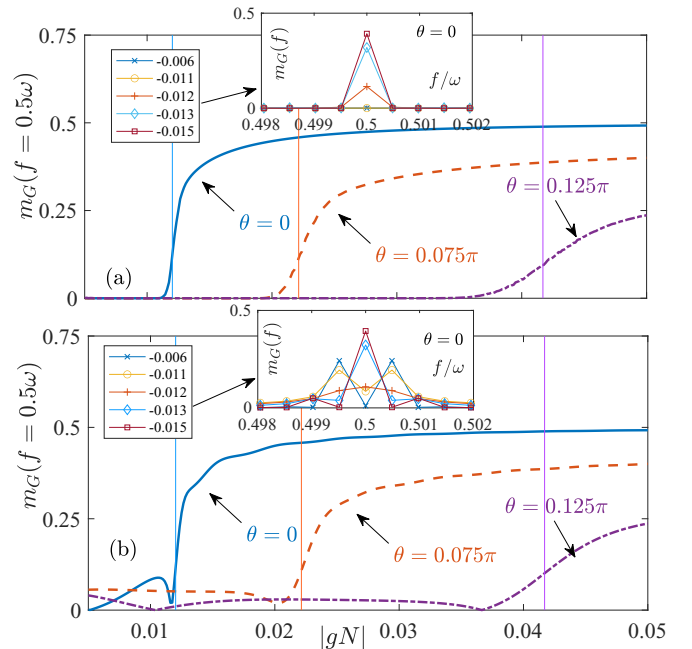

FIG. 6. (a) Subharmonic response $|m_G(f = 0.5\omega)|$ of the steady state [at $t = k_0 T$ to $(k_0 + 2048)T$ with $k_0 = 10^5$] as a function of gN for different initial states $|\{\theta, \varphi = 0\}\rangle$ defined in Eq. (11) with $\theta = 0$, 0.075π, and 0.125π shown by the blue solid, red dashed, and purple dashed-dotted curves, respectively. The thin vertical lines indicate the critical interaction $|g_c N|$. The inset shows the frequency response in the window near 0.5ω for different gN indicated in the legend. (b) The same as (a) for the transient state at $t = 0T$ to $2048T$.
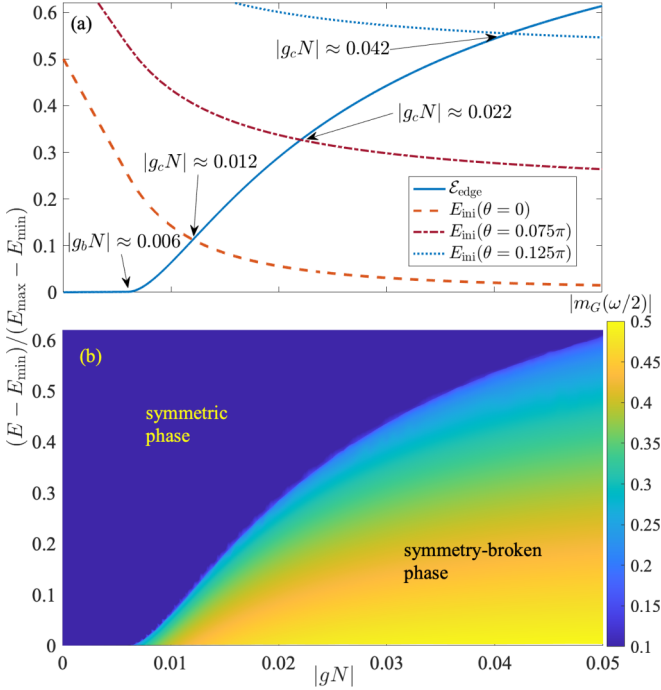
FIG. 7. (a) $\mathcal{E}_{\text{edge}}$ (blue solid curve) as a function of $|gN|$ and the initial energy $E_{\text{ini}}(\theta) \equiv E_{\text{ini}}(\theta, \varphi = 0)$ as a function of $|gN|$ for different initial states $|\Theta(0)\rangle = |\{\theta, \varphi = 0\}\rangle$ with $\theta = 0,\ 0.075\pi$, and 0.125π (red dashed, purple dashed-dotted, and light blue dotted, respectively). The initial energy curve crosses the edge at the critical $|g_cN|$ shown in Fig. 6. (b) Subharmonic response $|m_G(\omega/2)|$ (color bar) as a function of normalized initial energy E_{ini} and gN for all initial states $|\{\theta, \varphi = 0\}\rangle$ [with $\theta \in [0, \pi)$], indicating the symmetry-broken and symmetric phases. This phase diagram also applies to other possible initial product states $|\{\theta, \varphi\}\rangle$, with the exception of some regions where the condition $\varphi \neq 0$ limits the range of $E_{\text{ini}}(\theta, \varphi)$ that can be accessed (see Appendix D for details regarding $\varphi \neq 0$ cases).

shown in Fig. 7(a). The inset of Fig. 6(a) shows the frequency response $|m_G(f)|$ for f close to $\omega/2$ and the initial state $|\Theta(0)\rangle = |\{\theta = 0, \varphi = 0\}\rangle = |0, N\rangle$. We can see that a single sharp peak appears abruptly when $|gN| \geqslant |g_cN|$. However, in realistic experiments, one might not be able to access such very long evolution times. In Fig. 6(b), we show that the transient behavior at relatively short times can be regarded as a precursor. One can see that, while not as smooth and clean as Fig. 6(a), $|m_G(\omega/2)|$ still shows an abrupt change to a much larger value near $|g_cN|$. In the inset, one can see that the frequency response of the transient states for $\theta = 0$ at short times shows a double-peak structure for $|gN| < |g_cN|$ and which changes to a single-peak structure for $|gN| \geqslant |g_cN|$, the same as the observation in [50]. In the steady-state regime, we now have the intriguing situation where, as the magnitude of the interaction is increased from that just below the critical interaction $|g_cN|$ to just above $|g_cN|$, the period of the bouncing atom cloud changes from period T to period $2T$, to form a DTC. Although the numerical results presented here are calculated for a finite $N = 1000$, we believe the conclusions remain valid in the thermodynamic limit ($N \to \infty$ and finite gN). An analysis of the finite-size effect is given in Appendix E.
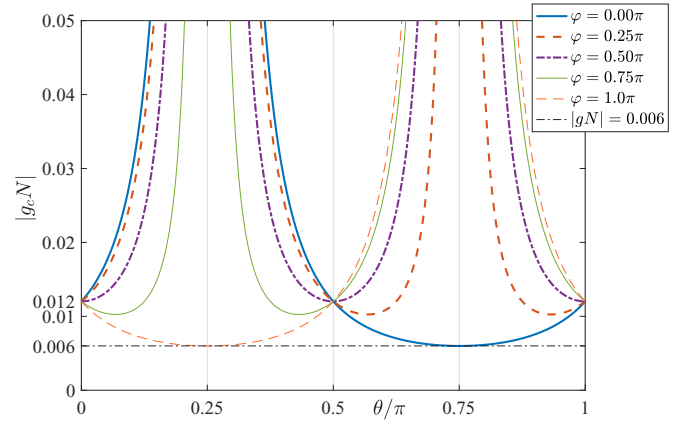

FIG. 8. $|g_cN|$ for different initial product states $|\{\theta, \varphi\}\rangle$. The minimum possible $|g_cN| \approx 0.006$ corresponds to $\{\theta, \varphi\} = \{0.75\pi, 0\}$ (or $\{0.25\pi, \pi\}$ which corresponds to the same physical state). The condition $\theta = 0$ ($\theta = \pi/2$) corresponds to the initial state being $|0, N_2 = N\rangle$ ($|N_1 = N, 0\rangle$), where φ is irrelevant and $|g_cN| \approx 0.012$.

The whole phase diagram for different initial energy and interaction strength is summarized in Fig. 7. The solid line in Fig. 7(a) shows the normalized $\mathcal{E}_{\text{edge}}$, which agrees with the phase boundary indicated by the subharmonic response $m_G(f = \omega/2)$ in Fig. 7(b). The dashed, dashed-dotted, and dotted curves in Fig. 7(a) show the initial energy $E_{\text{ini}}(\theta, \varphi = 0)$ as a function of $|gN|$ for different initial states $|\Theta(0)\rangle = |\{\theta, \varphi = 0\}\rangle$ defined in Eq. (11) with $\theta = 0,\ 0.075\pi$, and 0.125π, respectively. The initial energy curve crosses the edge at the critical $|g_cN|$ shown in Fig. 6. For a general initial product state $|\{\theta, \varphi\}\rangle$, the critical $|g_cN|$ as a function of θ for a given φ is shown in Fig. 8. (See Appendix D for details.) This shows that the onset of DTC formation depends on the choice of initial state (θ, φ) through the initial energy $E_{\text{ini}}(\theta, \varphi)$, as well as on the system parameters J, N. Here, the critical $|g_cN|$ for the onset of DTC formation is determined by equating the initial energy $E_{\text{ini}}(\theta, \varphi)$ with the E_{edge}.

These phase diagrams indicate that the symmetry of the steady state characterized by the subharmonic response $|m_G(\omega/2)|$ is determined by whether the initial energy is above or below the symmetry-breaking edge of the eigenenergy spectrum for a given interaction strength gN. The symmetry-breaking edge thus gives the abrupt phase transition boundary. This phase transition boundary is valid for any general initial product states $|\{\theta, \varphi\}\rangle$ (see Appendix D for details).

This $\mathbb{Z}_2$ symmetry breaking is associated with the time-translational symmetry breaking in the time crystal. Denoting the elements of the eigenstate vector $\vec{f}_\nu$ as $f_n^{(\nu)}$, the eigenstates can be written as $|\nu; t\rangle = \sum_n f_n^{(\nu)}|n, N - n; t\rangle$. The permutation operator $\hat{P}_{12}|n, N - n; t\rangle = |N - n, n; t\rangle$ transforms the eigenstates as

$$\hat{P}_{12}|\nu; t\rangle = \sum_n f_n^{(\nu)}|N - n, n; t\rangle$$

$$= \sum_n f_n^{(\nu)}|n, N - n; t + T\rangle = |\nu; t + T\rangle. \quad (23)$$

For $\mathbb{Z}_2$ symmetry-unbroken eigenstates, we also have $\hat{P}_{12}|\nu;t\rangle_S = \pm|\nu;t\rangle_S$, which leads to $|\nu;t+T\rangle_S = \pm|\nu;t\rangle_S$. Therefore, these eigenstates are T periodic, and satisfy the same discrete time-translational symmetry as the Hamiltonian. In contrast, for a pair of $\mathbb{Z}_2$ symmetry-broken approximate eigenstates, we have $\hat{P}_{12}|\nu;t\rangle_U = |\nu;t\rangle_L = |\nu;t+T\rangle_U \neq |\nu;t\rangle_U$. These eigenstates therefore have a period of $2T$ instead of T, which breaks the discrete time-translational symmetry of the Hamiltonian. The eigenstates of $\hat{h}_0$ can be regarded as an approximation of the many-body Floquet states in Eq. (9) with period $2T$. Therefore, the near-degeneracy of $|\nu\rangle_L$ and $|\nu\rangle_U$ in the symmetry-breaking regime plays the same role as the nearly π pairing of T-Floquet states in MBL and many-body quantum scar DTCs [27].

V. SUMMARY

We have derived a two-mode model from standard quantum field theory to study discrete time-translational symmetry breaking and the formation of DTCs in a Bose-Einstein condensate bouncing resonantly on an oscillating mirror. The validity of this simple many-body model has been investigated by comparing with previous multimode phase-space many-body calculations based on the TWA approach [50]. The greatly reduced computational times using this simple many-body model allow us to study the long-time dynamical evolution of the many-body system. Using two Wannier modes constructed from two single-particle Floquet states, the dynamical evolution has been studied both via a fully time-dependent Floquet Hamiltonian (MBF) and by using a time-independent Hamiltonian based on a high-frequency expansion (HFE). In the HFE approach, the Hamiltonian is equivalent to the Lipkin-Meshkov-Glick model [49,55,56]. The main initial state chosen has all bosons in the Wannier mode that closely resembles the condensate mode for a BEC in a harmonic trap treated in our TWA approach. However, a wide variety of initial states based on the two Wannier modes has also been studied. A new criterion for demonstrating the periodicity at stroboscopic times has been developed which involves the mean number of bosons in each Wannier mode.

We find that the evolution investigated in previous studies in the time window out to about 2000 driving periods actually involves "short-time" transient phenomena though DTC formation is still shown if the interboson interaction is strong enough. The two-mode approach compares well with the TWA approach in regard to the critical $|g_cN|$ for DTC formation. However the TWA treatment is needed to verify that quantum depletion to other modes is negligible. After much longer evolution times, initial states with no long-range correlations relax to a steady state and eventually show short-lived quantum revivals. In the steady state the mean boson number in each Wannier mode demonstrates that stroboscopic DTC behavior occurs for the same interaction regime found in the previous TWA calculations, the critical value for DTC formation with $2T$ periodicity being about $g_cN = -0.012$ for the parameters considered and the initial state $|\{\theta = 0, \varphi = 0\}\rangle$, which is the easiest to prepare in an experiment. However, the two-mode theory now more clearly shows that in the steady-state regime, for the initial state $|\{\theta = 0, \varphi = 0\}\rangle$ and for smaller $|gN|$, only T periodicity occurs.

For a general initial product state condition $\{\theta, \varphi\}$, the magnitude of the critical value $|g_cN|$ can be as low as -0.006 (see Fig. 8 and Appendix D). The long-time behavior can be understood via the many-body Floquet quasieigenenergy spectrum of the two-mode model. For sufficiently strong interaction, a symmetry-breaking edge appears in the spectrum, where all quasieigenstates below the edge are symmetry breaking while those above the edge are symmetric. The position of the edge is found to depend on the boson number and the intermode tunneling rate, and gives g_cN as a function of E_{ini} without explicit dependence on initial details $\{\theta, \varphi\}$. Finally, a phase diagram showing regions of symmetry-broken and symmetric phases for differing initial energies and interaction strengths summarizes the subharmonic response results. Here, we now allow for initial states where all bosons occupy a mode which is a linear combination of the two Wannier modes parametrized by $\{\theta, \varphi\}$. Our results predict that in the steady-state regime, after about 50 000 driving periods (for the parameters considered), as the magnitude of the interaction is increased from just below to just above the critical interaction strength the period of the bouncing atom cloud changes abruptly from the driving period T to period $2T$, to form a discrete time crystal. The present two-mode theory approach predicts that the discrete time crystal survives for times out to 250 000 driving periods. However, after astronomically long time, the escape of atoms to other modes beyond our two-mode model might eventually occur, leading to a finite lifetime of our long-lived DTC.

APPENDIX A: DERIVATIONS

In this Appendix we derive some of the key equations used in the main body of the paper.

1. Derivation of Eqs. (8) and (9)

Substituting the two-mode expansion (5) of the field operators into the Hamiltonian in Eq. (1) gives

$$\hat{H}_{2m} = \sum_{i,j=1,2} E_{i,j}\hat{a}_i^\dagger\hat{a}_j + \frac{g}{2}\sum_{i,j,k,l=1,2} U_{i,j,k,l}\hat{a}_i^\dagger\hat{a}_j^\dagger\hat{a}_k\hat{a}_l, \quad \text{(A1)}$$

where

$$E_{i,j} = \int dz\,\Phi_i(z,t)^* H_{sp}\Phi_j(z,t), \quad \text{(A2)}$$

$$U_{i,j,k,l} = \int dz\,\Phi_i(z,t)^*\Phi_j(z,t)^*\Phi_k(z,t)\Phi_l(z,t). \quad \text{(A3)}$$

Using Eq. (4) for the Wannier modes and Eq. (3) for the Floquet modes we then find that

$$E_{1,1} = (\epsilon_1 + \epsilon_2 - \hbar\omega/2)/2 - \hbar D_{1,1} = \epsilon_{1,1} - \hbar D_{1,1},$$

$$E_{1,2} = (\epsilon_1 - \epsilon_2 + \hbar\omega/2)/2 - \hbar D_{1,2} = \epsilon_{1,2} - \hbar D_{1,2},$$

$$E_{2,1} = (\epsilon_1 - \epsilon_2 + \hbar\omega/2)/2 - \hbar D_{2,1} = \epsilon_{2,1} - \hbar D_{2,1},$$
$$E_{2,2} = (\epsilon_1 + \epsilon_2 - \hbar\omega/2)/2 - \hbar D_{2,2} = \epsilon_{2,2} - \hbar D_{2,2}, \quad \text{(A4)}$$

where

$$D_{j,i} = -i \int dz\, \Phi_j(z,t)^* \frac{\partial}{\partial t} \Phi_i(z,t) = D_{i,j}^*, \quad \text{(A5)}$$

$$\epsilon_{1,1} = \epsilon_{2,2} = (\epsilon_1 + \epsilon_2 - \hbar\omega/2)/2 = \epsilon, \quad \text{(A6)}$$

$$\epsilon_{1,2} = \epsilon_{2,1} = (\epsilon_1 - \epsilon_2 + \hbar\omega/2)/2 = J. \quad \text{(A7)}$$

Hence, the Hamiltonian is given by

$$\hat{H}_{2m} = \sum_{i,j=1,2} (\epsilon_{i,j} - \hbar D_{i,j})\hat{a}_i^\dagger \hat{a}_j + \frac{g}{2} \sum_{i,j,k,l=1,2} U_{i,j,k,l}\hat{a}_i^\dagger \hat{a}_j^\dagger \hat{a}_k \hat{a}_l. \quad \text{(A8)}$$

We now expand the quantum state as

$$|\Theta(t)\rangle = \sum_n B_n(t)|n, N-n\rangle, \quad \text{(A9)}$$

where $|n_1, n_2\rangle$ are Fock states given by Eq. (6), with n_1, n_2 bosonic atoms in modes Φ_1, Φ_2, respectively. Note that these basis states are time dependent, as are the amplitudes $B_n(t)$.

Substituting into the time-dependent Schrödinger equation then gives

$$\sum_m B_m(t)\hat{H}_{2m}|m, N-m\rangle = i\hbar \sum_n \left(\frac{\partial}{\partial t}B_n(t)\right)|n, N-n\rangle$$
$$+ i\hbar \sum_m B_m(t)\left(\frac{\partial}{\partial t}|m, N-m\rangle\right), \quad \text{(A10)}$$

so taking the scalar product with $\langle n, N-n|$ on each side gives

$$i\hbar\left(\frac{\partial}{\partial t}B_n(t)\right) = \sum_m B_m(t)\langle n, N-n|\hat{H}_{2m}|m, N-m\rangle$$
$$- i\hbar \sum_m B_m(t)\langle n, N-n|\left(\frac{\partial}{\partial t}|m, N-m\rangle\right). \quad \text{(A11)}$$

We can eliminate the $D_{i,j}$ terms by using the expansion for the time-independent field creation operator to first derive an equation for the time derivative of the Wannier mode creation operators

$$0 = \sum_i \Phi_i(z,t)^* \frac{\partial}{\partial t}\hat{a}_i^\dagger + \sum_j \frac{\partial}{\partial t}\Phi_j(z,t)^*\hat{a}_j^\dagger,$$
$$\frac{\partial}{\partial t}\hat{a}_i^\dagger = -\sum_j \int dz\left(\Phi_i(z,t)\frac{\partial}{\partial t}\Phi_j(z,t)^*\right)\hat{a}_j^\dagger = i\sum_j D_{j,i}\hat{a}_j^\dagger. \quad \text{(A12)}$$

Hence, the time derivative of the basis states is

$$\frac{\partial}{\partial t}|n_1, n_2\rangle = \left\{\left(\frac{\partial}{\partial t}(\hat{a}_1^\dagger)^{n_1}\right)(\hat{a}_2^\dagger)^{n_2} + (\hat{a}_1^\dagger)^{n_1}\left(\frac{\partial}{\partial t}(\hat{a}_2^\dagger)^{n_2}\right)\right\}|0,0\rangle/(\sqrt{n_1!}\sqrt{n_2!})$$
$$= \left\{n_1(\hat{a}_1^\dagger)^{n_1-1}\left(\frac{\partial}{\partial t}(\hat{a}_1^\dagger)\right)(\hat{a}_2^\dagger)^{n_2} + (\hat{a}_1^\dagger)^{n_1}n_2(\hat{a}_2^\dagger)^{n_2-1}\left(\frac{\partial}{\partial t}(\hat{a}_2^\dagger)\right)\right\}|0,0\rangle/(\sqrt{n_1!}\sqrt{n_2!})$$
$$= \left\{n_1(\hat{a}_1^\dagger)^{n_1-1}i\sum_j D_{j,1}\hat{a}_j^\dagger(\hat{a}_2^\dagger)^{n_2} + (\hat{a}_1^\dagger)^{n_1}n_2(\hat{a}_2^\dagger)^{n_2-1}i\sum_j D_{j,2}\hat{a}_j^\dagger\right\}|0,0\rangle/(\sqrt{n_1!}\sqrt{n_2!})$$
$$= i\{n_1(\hat{a}_1^\dagger)^{n_1}D_{1,1}(\hat{a}_2^\dagger)^{n_2} + (\hat{a}_1^\dagger)^{n_1+1}n_2(\hat{a}_2^\dagger)^{n_2-1}D_{1,2}\}|0,0\rangle/(\sqrt{n_1!}\sqrt{n_2!})$$
$$+ i\{n_1 D_{2,1}(\hat{a}_1^\dagger)^{n_1-1}(\hat{a}_2^\dagger)^{n_2+1} + n_2 D_{2,2}(\hat{a}_1^\dagger)^{n_1}(\hat{a}_2^\dagger)^{n_2}\}|0,0\rangle/(\sqrt{n_1!}\sqrt{n_2!})$$
$$= i\{n_1 D_{1,1}|n_1, n_2\rangle + \sqrt{n_1+1}\sqrt{n_2}D_{1,2}|n_1+1, n_2-1\rangle\}$$
$$+ i\{\sqrt{n_1}\sqrt{n_2+1}D_{2,1}|n_1-1, n_2+1\rangle + n_2 D_{2,2}|n_1, n_2\rangle\}$$
$$= i\{D_{1,1}\hat{a}_1^\dagger \hat{a}_1 + D_{1,2}\hat{a}_1^\dagger \hat{a}_2 + D_{2,1}\hat{a}_2^\dagger \hat{a}_1 + D_{2,2}\hat{a}_2^\dagger \hat{a}_2\}|n_1, n_2\rangle$$
$$= \left(\sum_{i,j} D_{i,j}\hat{a}_i^\dagger \hat{a}_j\right)|n_1, n_2\rangle, \quad \text{(A13)}$$

where we have used the result that the $\partial_t \hat{a}_i^\dagger$ commute with any $\hat{a}_j^\dagger$.

Hence on substituting for $(\frac{\partial}{\partial t}|m, N-m\rangle)$ in Eq. (A11) we see that the $D_{i,j}$ terms cancel out leaving

$$i\hbar\left(\frac{\partial}{\partial t}B_n(t)\right) = \sum_m B_m(t)\langle n, N-n|\left(\sum_{i,j=1,2}\epsilon_{i,j}\hat{a}_i^\dagger \hat{a}_j + \frac{g}{2}\sum_{i,j,k,l=1,2}U_{i,j,k,l}\hat{a}_i^\dagger \hat{a}_j^\dagger \hat{a}_k \hat{a}_l\right)|m, N-m\rangle. \quad \text{(A14)}$$

If we write $B_n(t) = b_n(t) \exp(-i\epsilon N t/\hbar)$ we then find that the terms involving ϵ cancel out leaving

$$i\hbar\left(\frac{\partial}{\partial t} b_n(t)\right) = \sum_m b_m(t)\langle n, N-n|\left[J(\hat{a}_1^\dagger \hat{a}_2 + \hat{a}_2^\dagger \hat{a}_1)\right.$$
$$\left. + \frac{g}{2}\sum_{i,j,k,l=1,2} U_{i,j,k,l}\hat{a}_i^\dagger \hat{a}_j^\dagger \hat{a}_k \hat{a}_l\right]|m, N-m\rangle,$$

(A15)

so we now have

$$\sum_m \langle n, N-n|(\hat{\mathcal{H}})|m, N-m\rangle b_m(t) - i\hbar\left(\frac{\partial}{\partial t} b_n(t)\right) = 0,$$

(A16)

$$\left(\underline{\mathcal{H}} - i\hbar\frac{\partial}{\partial t}\right)\vec{b} = 0,$$

(A17)

where

$$\hat{\mathcal{H}} = J(\hat{a}_1^\dagger \hat{a}_2 + \hat{a}_2^\dagger \hat{a}_1) + \frac{g}{2}\sum_{i,j,k,l=1,2} U_{i,j,k,l}\hat{a}_i^\dagger \hat{a}_j^\dagger \hat{a}_k \hat{a}_l$$

(A18)

and the quantum state is now given by

$$|\Theta(t)\rangle = \exp(-i\epsilon N t/\hbar)\sum_n b_n(t)|n, N-n\rangle.$$

(A19)

The phase factor $\exp(-i\epsilon N t/\hbar)$ is not physically important. Thus, Eqs. (A17) and (A18) are equivalent to Eqs. (7) and (8) in the main part of the paper after introducing the matrix $\underline{\mathcal{H}}$ for $\hat{\mathcal{H}}$ and a column vector $\vec{b}$ for the amplitudes $b_n(t)$ via $\underline{\mathcal{H}}_{nm} = \langle n, N-n|\hat{\mathcal{H}}|m, N-m\rangle$ and $\vec{b}_n = b_n(t)$.

2. Derivation of Eq. (18)

At this stage the HFE approximation has been made, so that $\hat{\mathcal{H}}$ is replaced by $\hat{h}_0$ given by

$$\hat{h}_0 = J(\hat{a}_1^\dagger \hat{a}_2 + \hat{a}_2^\dagger \hat{a}_1) + \frac{g}{2}\sum_{i,j,k,l=1,2} \bar{U}_{i,j,k,l}\hat{a}_i^\dagger \hat{a}_j^\dagger \hat{a}_k \hat{a}_l,$$

(A20)

$$\bar{U}_{i,j,k,l} = \frac{1}{2T}\int dt\, U_{i,j,k,l},$$

(A21)

which now means that all the coefficients in $\hat{h}_0$ are time independent.

Many of the 16 coefficients $\bar{U}_{i,j,k,l}$ are inter-related. First, from the definition of $U_{i,j,k,l}$ we see that

$$\bar{U}_{i,j,k,l} = \bar{U}_{j,i,k,l} = \bar{U}_{i,j,l,k},$$

(A22)

which leads to

$$\begin{aligned}
\bar{U}_{11,12} &= \bar{U}_{11,21} & \bar{U}_{22,12} &= \bar{U}_{22,21}, \\
\bar{U}_{12,11} &= \bar{U}_{21,11} & \bar{U}_{12,22} &= \bar{U}_{21,22}, \\
\bar{U}_{12,12} &= \bar{U}_{12,21} = \bar{U}_{21,12} = \bar{U}_{21,21}.
\end{aligned}$$

(A23)

In addition to these 12 coefficients, there are 4 more, namely, $\bar{U}_{11,22}, \bar{U}_{22,11}, \bar{U}_{11,11}$, and $\bar{U}_{22,22}$.

We can show more inter-relationships by expressing the Wannier states by introducing the notation $\eta(t) = \exp(-i\pi t/T)$ and $s_i = 1$ for Wannier mode Φ_1 and $s_i = -1$ for Wannier mode Φ_2. Thus, $\Phi_i(z, t) = a(\phi_1(z, t) +$

$s_i\eta(t)\phi_2(z, t))$, where $a = 1/\sqrt{2}$. We can then divide the time interval 0 to $2T$ in the definition for $\bar{U}_{i,j,k,l}$ into time intervals 0 to T and T to $2T$, and then make use of the properties $\phi_i(z, t+T) = \phi_i(z, t)$ and $\eta(t+T) = -\eta(t)$ to convert the integral from T to $2T$ back into an integral from 0 to T. This gives the following expression for $\bar{U}_{i,j,k,l}$:

$$\bar{U}_{i,j,k,l} = \frac{a^4}{2T}\int_0^T dt \int dz\left(\begin{matrix}(\phi_1^* + s_i\eta^*\phi_2^*)(\phi_1^* + s_j\eta^*\phi_2^*) \\ \times(\phi_1 + s_k\eta\phi_2)(\phi_1 + s_l\eta\phi_2)\end{matrix}\right)$$
$$+ \frac{a^4}{2T}\int_0^T dt \int dz\left(\begin{matrix}(\phi_1^* - s_i\eta^*\phi_2^*)(\phi_1^* - s_j\eta^*\phi_2^*) \\ \times(\phi_1 - s_k\eta\phi_2)(\phi_1 - s_l\eta\phi_2)\end{matrix}\right),$$

(A24)

where the z, t dependence of the functions is left understood. This enables us to establish more inter-relationships, as the second term for one $\bar{U}_{i,j,k,l}$ is often the first term for another $\bar{U}_{i,j,k,l}$, and vice versa. Hence, we find that

$$\begin{aligned}
\bar{U}_{11,11} &= \bar{U}_{22,22}, & \bar{U}_{11,22} &= \bar{U}_{22,11}, \\
\bar{U}_{22,21} &= \bar{U}_{11,12}, & \bar{U}_{12,11} &= \bar{U}_{21,22}.
\end{aligned}$$

(A25)

Also, we see from Eq. (A24) that there is a further relationship

$$\bar{U}_{i,j,k,l}^* = \bar{U}_{k,l,i,j},$$

(A26)

which leads to

$$\bar{U}_{12,11} = \bar{U}_{11,12}^* = \bar{U}_{11,12}$$

(A27)

since we can show that

$$\bar{U}_{11,12} = \frac{a^4}{T}\int_0^T dt \int dz |\phi_1 + \eta\phi_2|^2(|\phi_1|^2 - |\phi_2|^2)$$

(A28)

is real.

Also, we have

$$\bar{U}_{12,12} = \frac{a^4}{T}\int_0^T dt \int dz(|\phi_1 + \eta\phi_2|^2 \mid \phi_1 - \eta\phi_2|^2)$$
$$\bar{U}_{11,22} = \frac{a^4}{T}\int_0^T dt \int dz\left(\begin{matrix}(|\phi_1|^2 - |\phi_2|^2)^2 \\ +(\eta\phi_1^*\phi_2 - \eta^*\phi_2^*\phi_1)^2\end{matrix}\right),$$
$$\bar{U}_{11,11} = \frac{a^4}{2T}\int_0^T dt \int dz(|\phi_1 + \eta\phi_2|^4 + |\phi_1 - \eta\phi_2|^4),$$

(A29)

which are all real.

Hence, overall we have only four independent coefficients which can be listed as

$$\begin{aligned}
u_T &= \bar{U}_{11,12} = \bar{U}_{11,21} = \bar{U}_{22,12} = \bar{U}_{22,21} \\
&= \bar{U}_{12,11} = \bar{U}_{21,11} = \bar{U}_{12,22} = \bar{U}_{21,22}, \\
u_N &= \bar{U}_{12,12} = \bar{U}_{12,21} = \bar{U}_{21,12} = \bar{U}_{21,21}, \\
u_P &= \bar{U}_{11,22} = \bar{U}_{22,11}, \\
u_I &= \bar{U}_{11,11} = \bar{U}_{22,22}.
\end{aligned}$$

(A30)

This obviously enables the expression for $\hat{h}_0$ to be simplified. Hence, we have

$$
\begin{aligned}
\hat{h}_0 = {}& J(\hat{a}_1^\dagger \hat{a}_2 + \hat{a}_2^\dagger \hat{a}_1) + \frac{g}{2} u_T \begin{pmatrix} \hat{a}_1^\dagger \hat{a}_1^\dagger \hat{a}_1 \hat{a}_2 + \hat{a}_1^\dagger \hat{a}_1^\dagger \hat{a}_2 \hat{a}_1 \\ + \hat{a}_2^\dagger \hat{a}_2^\dagger \hat{a}_1 \hat{a}_2 + \hat{a}_2^\dagger \hat{a}_2^\dagger \hat{a}_2 \hat{a}_1 \\ + \hat{a}_1^\dagger \hat{a}_2^\dagger \hat{a}_1 \hat{a}_1 + \hat{a}_2^\dagger \hat{a}_1^\dagger \hat{a}_1 \hat{a}_1 \\ + \hat{a}_1^\dagger \hat{a}_2^\dagger \hat{a}_2 \hat{a}_2 + \hat{a}_2^\dagger \hat{a}_1^\dagger \hat{a}_2 \hat{a}_2 \end{pmatrix} \\
& + \frac{g}{2} u_N \begin{pmatrix} \hat{a}_1^\dagger \hat{a}_2^\dagger \hat{a}_1 \hat{a}_2 + \hat{a}_1^\dagger \hat{a}_2^\dagger \hat{a}_2 \hat{a}_1 \\ + \hat{a}_2^\dagger \hat{a}_1^\dagger \hat{a}_1 \hat{a}_2 + \hat{a}_2^\dagger \hat{a}_1^\dagger \hat{a}_2 \hat{a}_1 \end{pmatrix} \\
& + \frac{g}{2} u_P (\hat{a}_1^\dagger \hat{a}_1^\dagger \hat{a}_2 \hat{a}_2 + \hat{a}_2^\dagger \hat{a}_2^\dagger \hat{a}_1 \hat{a}_1) \\
& + \frac{g}{2} u_I (\hat{a}_1^\dagger \hat{a}_1^\dagger \hat{a}_1 \hat{a}_1 + \hat{a}_2^\dagger \hat{a}_2^\dagger \hat{a}_2 \hat{a}_2) \\
= {}& J(\hat{a}_1^\dagger \hat{a}_2 + \hat{a}_2^\dagger \hat{a}_1) + g u_T (\hat{a}_1^\dagger \hat{N} \hat{a}_2 + \hat{a}_2^\dagger \hat{N} \hat{a}_1) \\
& + \frac{g}{2} u_N (4 \hat{N}_1 \hat{N}_2) + \frac{g}{2} u_P (\hat{a}_1^\dagger \hat{a}_1^\dagger \hat{a}_2 \hat{a}_2 + \hat{a}_2^\dagger \hat{a}_2^\dagger \hat{a}_1 \hat{a}_1) \\
& + \frac{g}{2} u_I [\hat{N}_1 (\hat{N}_1 - 1) + \hat{N}_2 (\hat{N}_2 - 1)], \qquad (A31)
\end{aligned}
$$

which is the same as Eq. (18).

3. Derivation of Lipkin-Meshkov-Glick Hamiltonian (21)

Here, we recast $\hat{h}_0$ in terms of bosonic spin operators defined as

$$
\begin{aligned}
\hat{S}_x &= (\hat{a}_2^\dagger \hat{a}_1 + \hat{a}_1^\dagger \hat{a}_2)/2, \\
\hat{S}_y &= (\hat{a}_2^\dagger \hat{a}_1 - \hat{a}_1^\dagger \hat{a}_2)/2i, \qquad (A32) \\
\hat{S}_z &= (\hat{a}_2^\dagger \hat{a}_2 - \hat{a}_1^\dagger \hat{a}_1)/2,
\end{aligned}
$$

which along with $\hat{N} = \hat{N}_1 + \hat{N}_2$ and the standard bosonic commutation rules for the mode annihilation and creation operators enable the following substitutions to be made within $\hat{h}_0$:

$$
\begin{aligned}
\hat{a}_1^\dagger \hat{a}_2 + \hat{a}_2^\dagger \hat{a}_1 &= 2\hat{S}_x, \\
\hat{N}_1 &= \tfrac{1}{2}\hat{N} - \hat{S}_z, \\
\hat{N}_2 &= \tfrac{1}{2}\hat{N} + \hat{S}_z, \\
\hat{a}_1^\dagger \hat{a}_2 &= \hat{S}_x - i\hat{S}_y, \\
\hat{a}_2^\dagger \hat{a}_1 &= \hat{S}_x + i\hat{S}_y, \\
\hat{a}_1^\dagger \hat{N} \hat{a}_2 &= \hat{a}_1^\dagger \hat{a}_2 (\hat{N} - 1) \\
&= (\hat{S}_x - i\hat{S}_y)(\hat{N} - 1), \\
\hat{a}_2^\dagger \hat{N} \hat{a}_1 &= (\hat{S}_x + i\hat{S}_y)(\hat{N} - 1). \qquad (A33)
\end{aligned}
$$

From Eq. (A31) we have

$$
\begin{aligned}
\hat{h}_0 = {}& J2\hat{S}_x \\
& + g u_T [(\hat{S}_x - i\hat{S}_y)(\hat{N} - 1) + (\hat{S}_x + i\hat{S}_y)(\hat{N} - 1)] \\
& + \frac{g}{2} u_N \left[4 \left(\frac{1}{2}\hat{N} - \hat{S}_z \right) \left(\frac{1}{2}\hat{N} + \hat{S}_z \right) \right] \\
& + \frac{g}{2} u_P [(\hat{S}_x - i\hat{S}_y)^2 + (\hat{S}_x + i\hat{S}_y)^2] \\
& + \frac{g}{2} u_I \left[\begin{array}{l} \left(\frac{1}{2}\hat{N} - \hat{S}_z \right)\left(\frac{1}{2}\hat{N} - \hat{S}_z - 1 \right) \\ + \left(\frac{1}{2}\hat{N} + \hat{S}_z \right)\left(\frac{1}{2}\hat{N} + \hat{S}_z - 1 \right) \end{array} \right]
\end{aligned}
$$

$$
\begin{aligned}
= {}& J2\hat{S}_x \\
& + g u_T 2\hat{S}_x (\hat{N} - 1) \\
& + \frac{g}{2} u_N \left[4 \left(\frac{1}{4}\hat{N}^2 - \hat{S}_z^2 \right) \right] \\
& + \frac{g}{2} u_P 2 (\hat{S}_x^2 - \hat{S}_y^2) \\
& + \frac{g}{2} u_I 2 \left[\left(\frac{1}{2}\hat{N} \right)\left(\frac{1}{2}\hat{N} - 1 \right) + \hat{S}_z^2 \right], \qquad (A34)
\end{aligned}
$$

so as we are only dealing with states which are eigenstates for the total boson number, we can replace $\hat{N}$ by N.

After combining similar terms we get

$$
\begin{aligned}
\hat{h}_0 = {}& 2[J + g u_T (N - 1)]\hat{S}_x \\
& + g(-2u_N + u_I)\hat{S}_z^2 \\
& + g u_P (\hat{S}_x^2 - \hat{S}_y^2) \\
& + \frac{gN}{2} \left[u_N N + u_I \left(\frac{1}{2}N - 1 \right) \right], \qquad (A35)
\end{aligned}
$$

which can be written as

$$
\hat{h}_0 = \tilde{J}\left(-\hat{S}_x + \frac{\gamma}{N}\hat{S}_z^2 \right) + E_{\text{shift}} + \beta \left(\hat{S}_x^2 - \hat{S}_y^2 \right), \qquad (A36)
$$

where

$$
\begin{aligned}
\tilde{J} &= -2[J + g u_T (N - 1)], \\
\gamma &= gN(-2u_N + u_I)/\tilde{J}, \\
E_{\text{shift}} &= \frac{gN}{2} \left[u_N N + u_I \left(\frac{1}{2}N - 1 \right) \right], \\
\beta &= g u_P. \qquad (A37)
\end{aligned}
$$

This is the same as Eq (21) in the main body of the paper, if the small term involving $\hat{S}_x^2 - \hat{S}_y^2$ is discarded.

APPENDIX B: MANY-BODY FLOQUET MODE SOLUTION

We can define many-body Floquet states $\vec{\mathcal{F}}_\nu$ and Floquet energies $\mathcal{E}_\nu$ as the solutions of the matrix equations [Eq. (10)]

$$
\left(\underline{\mathcal{H}} - i\hbar \frac{\partial}{\partial t} \right) \vec{\mathcal{F}}_\nu = \mathcal{E}_\nu \vec{\mathcal{F}}_\nu. \qquad (B1)
$$

It can then be confirmed that a solution for the amplitudes $b_n(t)$ can be found in the form

$$
\vec{b} = \sum \mathcal{C}_\nu \exp\left(-i\mathcal{E}_\nu t/\hbar \right) \vec{\mathcal{F}}_\nu, \qquad (B2)
$$

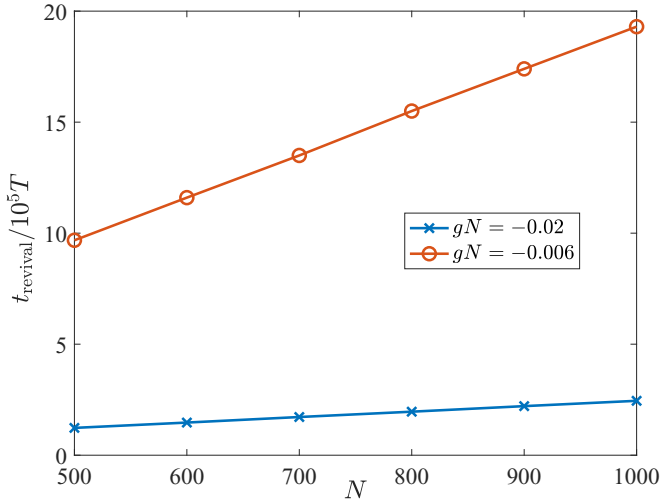where the $\mathcal{C}_\nu$ are time independent.

FIG. 9. The revival time as a function of particle number N. The blue crosses (red circles) show the revival time for $gN = -0.02$ (-0.006), respectively. The initial state is given by $|0, N\rangle$.

Substituting for $\vec{b}$ from Eq. (B2) into Eq. (A16) gives

$$
\begin{aligned}
\left(\underline{\mathcal{H}} - i\hbar \frac{\partial}{\partial t}\right)\vec{b} &= \sum_\nu \mathcal{C}_\nu \exp\left(-i\mathcal{E}_\nu t/\hbar\right)\left(\underline{\mathcal{H}} - i\hbar \frac{\partial}{\partial t}\right)\vec{\mathcal{F}}_\nu \\
&\quad - \sum_\nu \mathcal{C}_\nu \left(i\hbar \frac{\partial}{\partial t} \exp\left(-i\mathcal{E}_\nu t/\hbar\right)\right)\vec{\mathcal{F}}_\nu \\
&= \sum_\nu \mathcal{C}_\nu \exp\left(-i\mathcal{E}_\nu t/\hbar\right)\mathcal{E}_\nu \vec{\mathcal{F}}_\nu \\
&\quad - \sum_\nu \mathcal{C}_\nu \exp\left(-i\mathcal{E}_\nu t/\hbar\right)\mathcal{E}_\nu \vec{\mathcal{F}}_\nu \\
&= 0 \qquad\qquad\qquad\qquad\qquad\qquad\text{(B3)}
\end{aligned}
$$

as required. The initial condition gives $\mathcal{C}_\nu = \vec{\mathcal{F}}_\nu^\dagger \cdot \vec{b}(0)$.

APPENDIX C: QUANTUM REVIVAL

The quantum revival time can be obtained from the spectrum [52,57]

$$
T_{\text{revival}} = \frac{2\pi\hbar}{|(d^2\mathcal{E}_\nu/d\nu^2)(\nu_0)|}, \qquad \text{(C1)}
$$

where $\mathcal{E}_\nu$ are understood to be taken from the same branch (so that there is no near degeneracy), and ν is the index for ascending eigenenergies. ν_0 indicates the closest $\mathcal{E}_{\nu_0}$ to the initial energy E_{ini}, and the second derivative can be approximated by $d^2\mathcal{E}_\nu/d\nu^2 \approx \mathcal{E}_{\nu-1} + \mathcal{E}_{\nu+1} - 2\mathcal{E}_\nu$. Interestingly, we numerically find that the revival time linearly depends on the particle number N, as shown in Fig. 9. In other words, in the infinite-N limit, the revival would not be accessible.

APPENDIX D: INITIAL PRODUCT STATES

For initial states $|\Theta(0)\rangle = |\{\theta, \varphi\}\rangle$ with $\theta \in [0, \pi)$ and $\varphi \in [0, \pi)$ given by Eq. (11), all atoms occupy the same mode $\Lambda_2 = \sin\theta e^{i\varphi}\Phi_1 + \cos\theta \Phi_2$, and hence the energy can be given by a mean-field approach in the large-N limit, i.e.,

by replacing the creation and annihilation operators in the Hamiltonian (18) via

$$
\hat{a}_1, \hat{a}_1^\dagger \rightarrow \sqrt{N}\sin\theta e^{\pm i\varphi}, \quad \hat{a}_2, \hat{a}_2^\dagger \rightarrow \sqrt{N}\cos\theta. \qquad \text{(D1)}
$$

Neglecting the small terms associated with u_P, the energy functional is given by

$$
\frac{E_{\text{ini}}(\theta, \varphi) - E_{\text{shift}}}{N} = -\frac{\tilde{J}}{2}\sin 2\theta \cos\varphi + \frac{\tilde{\gamma}}{4}\cos^2 2\theta, \qquad \text{(D2)}
$$

where $\tilde{\gamma} = gN(u_I - 2u_N)$. Inserting the definitions of $\tilde{J}$ and E_{shift} given in the main text

$$
\tilde{J} = -2[J + gu_T(N-1)] \approx -2[J + gNu_T] \qquad \text{(D3)}
$$

and

$$
\frac{E_{\text{shift}}}{N} = \frac{1}{2}gN\left(\frac{u_I}{2} - \frac{u_I}{N} + u_N\right) \approx \frac{1}{2}gN\left(\frac{u_I}{2} + u_N\right) \qquad \text{(D4)}
$$

leads to

$$
\begin{aligned}
\frac{E_{\text{ini}}(\theta, \varphi)}{N} &\approx J\sin 2\theta \cos(\varphi) + gN\left[\frac{u_I}{2} + u_T\sin 2\theta \cos(\varphi)\right. \\
&\quad \left. + \frac{(2u_N - u_I)}{4}\sin^2 2\theta\right], \qquad \text{(D5)}
\end{aligned}
$$

which agrees with Eq. (22) in the main text. Equating $E_{\text{ini}}(\theta, \varphi)$ [given in Eq. (22) or (D5)] with the broken-symmetry edge [given in Eq. (20)] leads to the critical interaction strength as a function of θ for a given φ:

$$
\begin{aligned}
&g_c(\theta; \varphi)N \\
&= -\frac{J(1 + \sin 2\theta \cos\varphi)}{(u_I/4 - u_N/2)\cos^2 2\theta + u_T(1 + \sin 2\theta \cos\varphi)}, \\
&\qquad\qquad\qquad\qquad\qquad\qquad\qquad\qquad \text{(D6)}
\end{aligned}
$$

which is shown in Fig. 8. It is also important to note that the phase diagram does not depend explicitly on $\{\theta, \varphi\}$, where the subharmonic response $|m_G(\omega/2)|$ is essentially zero (nonzero) for $E_{\text{ini}}(\theta, \varphi) > E_{\text{edge}}$ [$E_{\text{ini}}(\theta, \varphi) \leqslant E_{\text{edge}}$] for a given $|gN|$. Figures 7(b), 10(a), and 10(b) show $|m_G(\omega/2)|$ for different initial states $|\{\theta, \varphi = 0\}\rangle$, $|\{\theta, \varphi = 0.25\pi\}\rangle$ and $|\{\theta, \varphi = 0.5\pi\}\rangle$, respectively, which agree with each other. However, the condition $\varphi \neq 0$ would limit the range of $E_{\text{ini}}(\theta, \varphi)$ that can be accessed, which is indicated by the white areas (no data) in Figs. 10(a) and 10(b).

In the large-N limit, since the spectrum is bounded from both below and above, the minimum and maximum energy state should also be well approximated by the mean-field expression, i.e., $E_{\text{max}} = \max[E_{\text{ini}}(\theta, \varphi)]$ and $E_{\text{min}} = \min[E_{\text{ini}}(\theta, \varphi)]$. These expressions are explicitly given by

$$
E_{\text{max}} \approx E_{\text{shift}} + \frac{|\tilde{J}|N}{2}, \qquad \text{(D7)}
$$

and for the negative gN considered in this work

$$
E_{\text{min}} \approx \begin{cases} E_{\text{shift}} - \frac{|\tilde{J}|N}{2}, & |\tilde{J}| \geqslant -\tilde{\gamma} \\ E_{\text{shift}} + N\left(\frac{\tilde{\gamma}}{4} + \frac{|\tilde{J}|^2}{4\tilde{\gamma}}\right), & |\tilde{J}| < -\tilde{\gamma} \end{cases} \qquad \text{(D8)}
$$

whose expression in the second line can also be explicitly written as $gN^2 u_I/2 + \tilde{J}^2 N/gN(u_I - 2u_N)$. In this work, we focus on the case $J + gNu_T > 0$, therefore, the critical
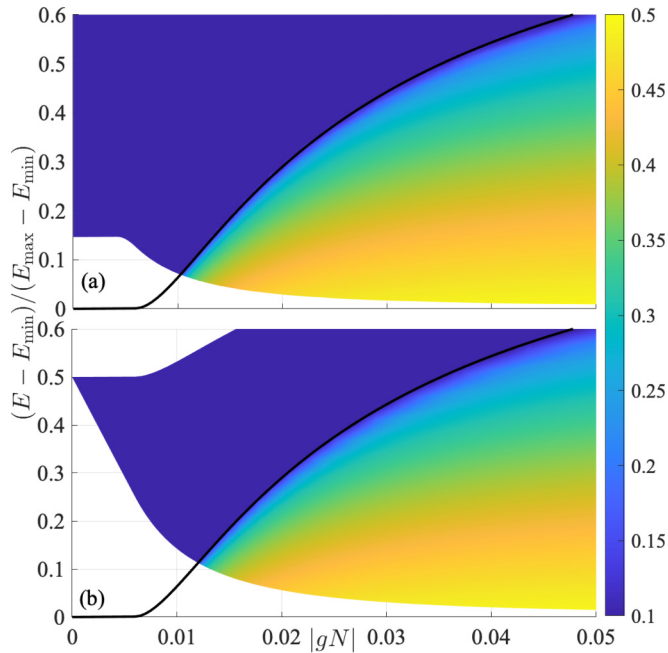
FIG. 10. Subharmonic response $|m_G(\omega/2)|$ (color bar) as a function of normalized E_{ini} and gN. The black curve shows the normalized $\mathcal{E}_{\text{edge}}$ as a function of $|gN|$, which coincides with the phase boundary for both initial product states $|\{\theta, \varphi = 0.25\pi\}\rangle$ in (a) and $|\{\theta, \varphi = 0.5\pi\}\rangle$ in (b).

condition gives

$$g_b N = -2J/(u_I - 2u_N + 2u_T). \tag{D9}$$

One can notice that the initial state corresponding to E_{min} actually corresponds to the "Wannier initial condition" in our previous study [50]. We also find here that the minimum value of $|g_c N|$ for DTC formation based on Wannier initial conditions is given by $|g_c N| = |g_b N| \approx 0.006$. This corresponds to $E_{\text{edge}} = E_{\text{min}}$ in Fig. 7(b).
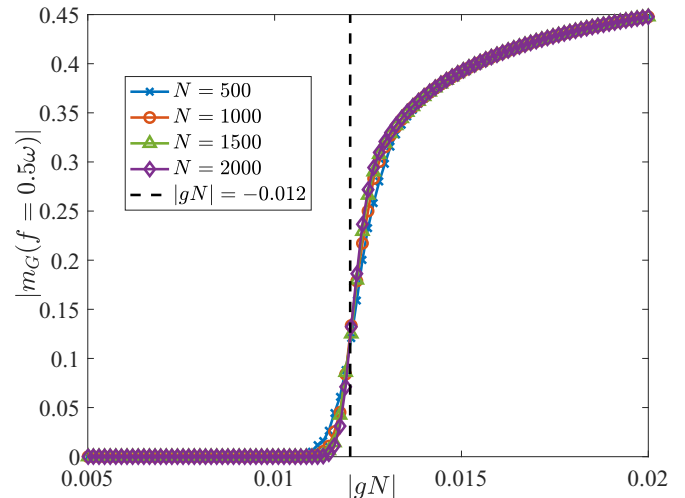

FIG. 11. Steady states' subharmonic response signal as a function of $|gN|$ for initial state $|0, N\rangle$ for different N denoted in the figure. The black dashed vertical line indicates the critical interaction strength $|gN| = 0.012$.

APPENDIX E: FINITE-SIZE EFFECT

In Ref. [40], it is noticed that the amplitude of the subharmonic response of a DTC in a many-body quantum scar system is exponentially suppressed with system size, and in principle would disappear in the thermodynamic limit. In contrast, the subharmonic response of a DTC in a MBL system does not decay with respect to system size. It is thus interesting to study the finite-size effect of our system, whose eigenspectra are different from both many-body quantum scar and MBL systems. Figure 11 shows the subharmonic response as a function of $|gN|$ for different N. We observe that the subharmonic response in the symmetry-broken phase does not decay with respect to N, similar to the DTC in MBL systems.

[1] F. Wilczek, Quantum Time Crystals, Phys. Rev. Lett. **109**, 160401 (2012).

[2] H. Watanabe and M. Oshikawa, Absence Of Quantum Time Crystals, Phys. Rev. Lett. **114**, 251603 (2015).

[3] V. K. Kozin and O. Kyriienko, Quantum Time Crystals From Hamiltonians With Long-Range Interactions, Phys. Rev. Lett. **123**, 210602 (2019).

[4] K. Sacha, Modeling spontaneous breaking of time-translation symmetry, Phys. Rev. A **91**, 033617 (2015).

[5] V. Khemani, A. Lazarides, R. Moessner, and S. L. Sondhi, Phase Structure Of Driven Quantum Systems, Phys. Rev. Lett. **116**, 250401 (2016).

[6] D. V. Else, B. Bauer, and C. Nayak, Floquet Time Crystals, Phys. Rev. Lett. **117**, 090402 (2016).

[7] N. Y. Yao, A. C. Potter, I.-D. Potirniche, and A. Vishwanath, Discrete Time Crystals: Rigidity, Criticality, And Realizations, Phys. Rev. Lett. **118**, 030401 (2017).

[8] J. Zhang, P. W. Hess, A. Kyprianidis, P. Becker, A. Lee, J. Smith, G. Pagano, I.-D. Potirniche, A. C. Potter, A. Vishwanath, N. Y. Yao, and C. Monroe, Observation of a discrete time crystal, Nature (London) **543**, 217 (2017).

[9] S. Choi, J. Choi, R. Landig, G. Kucsko, H. Zhou, J. Isoya, F. Jelezko, S. Onoda, H. Sumiya, V. Khemani, C. von Keyserlingk, N. Y. Yao, E. Demler, and M. D. Lukin, Observation of a discrete time crystal, Nature (London) **543**, 221 (2017).

[10] J. Rovny, R. L. Blum, and S. E. Barrett, Observation Of Discrete-Time-Crystal Signatures In An Ordered Dipolar Many-Body System, Phys. Rev. Lett. **120**, 180603 (2018).

[11] S. Pal, N. Nishad, T. S. Mahesh, and G. J. Sreejith, Temporal Order In Periodically Driven Spins In Star-Shaped Clusters, Phys. Rev. Lett. **120**, 180602 (2018).

[12] J. Rovny, R. L. Blum, and S. E. Barrett, ^{31}P NMR study of discrete time-crystalline signatures in an ordered crystal of ammonium dihydrogen phosphate, Phys. Rev. B **97**, 184301 (2018).

[13] J. Smits, L. Liao, H. T. C. Stoof, and P. van der Straten, Observation Of A Space-Time Crystal In A Superfluid Quantum Gas, Phys. Rev. Lett. **121**, 185301 (2018).

[14] L. Liao, J. Smits, P. van der Straten, and H. T. C. Stoof, Dynamics of a space-time crystal in an atomic Bose-Einstein condensate, Phys. Rev. A **99**, 013625 (2019).

[15] J. Smits, H. T. C. Stoof, and P. van der Straten, On the long-term stability of space-time crystals, New J. Phys. **22**, 105001 (2020).

[16] D. V. Else, B. Bauer, and C. Nayak, Prethermal Phases Of Matter Protected By Time-Translation Symmetry, Phys. Rev. X **7**, 011026 (2017).

[17] A. Russomanno, F. Iemini, M. Dalmonte, and R. Fazio, Floquet time crystal in the Lipkin-Meshkov-Glick model, Phys. Rev. B **95**, 214307 (2017).

[18] P. Matus and K. Sacha, Fractional time crystals, Phys. Rev. A **99**, 033626 (2019).

[19] B. Zhu, J. Marino, N. Y. Yao, M. D. Lukin, and E. A. Demler, Dicke time crystals in driven-dissipative quantum many-body systems, New J. Phys. **21**, 073028 (2019).

[20] F.-X. Sun, Q. He, Q. Gong, R. Y. Teh, M. D. Reid, and P. D. Drummond, Discrete time symmetry breaking in quantum circuits: Exact solutions and tunneling, New J. Phys. **21**, 093035 (2019).

[21] F. Machado, D. V. Else, G. D. Kahanamoku-Meyer, C. Nayak, and N. Y. Yao, Long-Range Prethermal Phases Of Nonequilibrium Matter, Phys. Rev. X **10**, 011043 (2020).

[22] M. Natsheh, A. Gambassi, and A. Mitra, Critical properties of the Floquet time crystal within the Gaussian approximation, Phys. Rev. B **103**, 014305 (2021).

[23] A. Pizzi, J. Knolle, and A. Nunnenkamp, Higher-order and fractional discrete time crystals in clean long-range interacting systems, Nat. Commun. **12**, 2341 (2021).

[24] K. Sacha and J. Zakrzewski, Time crystals: A review, Rep. Prog. Phys. **81**, 016401 (2018).

[25] V. Khemani, R. Moessner, and S. L. Sondhi, A brief history of time crystals, arXiv:1910.10745.

[26] D. V. Else, C. Monroe, C. Nayak, and N. Yao, Discrete time crystals, Ann. Rev. Condens. Matter Phys. **11**, 467 (2020).

[27] K. Sacha, *Time Crystals* (Springer, Berlin, 2020).

[28] L. D'Alessio and M. Rigol, Long-Time Behavior Of Isolated Periodically Driven Interacting Lattice Systems, Phys. Rev. X **4**, 041048 (2014).

[29] A. Lazarides, A. Das, and R. Moessner, Equilibrium states of generic quantum systems subject to periodic driving, Phys. Rev. E **90**, 012110 (2014).

[30] P. Ponte, A. Chandrana, Z. Papić, and D. A. Abanin, Periodically driven ergodic and many-body localized quantum systems, Ann. Phys. **353**, 196 (2015).

[31] P. Ponte, Z. Papić, F. Huveneers, and D. A. Abanin, Many-Body Localization In Periodically Driven Systems, Phys. Rev. Lett. **114**, 140401 (2015).

[32] A. Lazarides, A. Das, and R. Moessner, Fate Of Many-Body Localization Under Periodic Driving, Phys. Rev. Lett. **115**, 030402 (2015).

[33] D. Abanin, W. De Roeck, and F. Huveneers, A theory of many-body localization in periodically driven systems, Ann. Phys. **372**, 1 (2016).

[34] T. Kuwahara, T. Mori, and K. Saito, Floquet-Magnus theory and generic transient dynamics in periodically driven many-body quantum systems, Ann. Phys. **367**, 96 (2016).

[35] E. Canovi, M. Kollar, and M. Eckstein, Stroboscopic prethermalization in weakly interacting periodically driven systems, Phys. Rev. E **93**, 012130 (2016).

[36] F. Machado, G. D. Kahanamoku-Meyer, D. V. Else, C. Nayak, and N. Y. Yao, Exponentially slow heating in short and long-range interacting Floquet systems, Phys. Rev. Research **1**, 033202 (2019).

[37] C. J. Turner, A. A. Michailidis, D. A. Abanin, M. Serbyn, and Z. Papić, Weak ergodicity breaking from quantum many-body scars, Nat. Phys. **14**, 745 (2018).

[38] A. A. Michailidis, C. J. Turner, Z. Papić, D. A. Abanin, and M. Serbyn, Slow Quantum Thermalization And Many-Body Revivals From Mixed Phase Space, Phys. Rev. X **10**, 011055 (2020).

[39] F. M. Surace, M. Votto, E. G. Lazo, A. Silva, M. Dalmonte, and G. Giudici, Exact many-body scars and their stability in constrained quantum chains, Phys. Rev. B **103**, 104302 (2021).

[40] A. Pizzi, D. Malz, G. De Tomasi, J. Knolle, and A. Nunnenkamp, Time crystallinity and finite-size effects in clean Floquet systems, Phys. Rev. B **102**, 214207 (2020).

[41] J. H. Shirley, Solution of the Schrödinger equation with a Hamiltonian periodic in time, Phys. Rev. **138**, B979 (1965).

[42] H. Sambe, Steady states and quasienergies of a quantum-mechanical system in an oscillating field, Phys. Rev. A **7**, 2203 (1973).

[43] A. Eckardt and E. Anisimovas, High-frequency approximation for periodically driven quantum systems from a Floquet-space perspective, New J. Phys. **17**, 093039 (2015).

[44] C. W. von Keyserlingk, V. Khemani, and S. L. Sondhi, Absolute stability and spatiotemporal long-range order in Floquet systems, Phys. Rev. B **94**, 085112 (2016).

[45] C. W. von Keyserlingk and S. L. Sondhi, Phase structure of one-dimensional interacting Floquet systems. ii. symmetry-broken phases, Phys. Rev. B **93**, 245146 (2016).

[46] R. Moessner and S. L. Sondhi, Equilibration and order in quantum Floquet matter, Nat. Phys. **13**, 424 (2017).

[47] K. Giergiel, A. Kosior, P. Hannaford, and K. Sacha, Time crystals: Analysis of experimental conditions, Phys. Rev. A **98**, 013613 (2018).

[48] K. Giergiel, T. Tran, A. Zaheer, A. Singh, A. Sidorov, K. Sacha, and P. Hannaford, Creating big time crystals with ultracold atoms, New J. Phys. **22**, 085004 (2020).

[49] A. Kuroś, R. Mukherjee, W. Golletz, F. Sauvage, K. Giergiel, F. Mintert, and K. Sacha, Phase diagram and optimal control for n-tupling discrete time crystal, New J. Phys. **22**, 095001 (2020).

[50] J. Wang, P. Hannaford, and B. J. Dalton, Many-body effects and quantum fluctuations for discrete time crystals in Bose-Einstein condensates, New J. Phys. **23**, 063012 (2021).

[51] M. Albiez, R. Gati, J. Fölling, S. Hunsmann, M. Cristiani, and M. K. Oberthaler, Direct Observation Of Tunneling And Non-linear Self-Trapping In A Single Bosonic Josephson Junction, Phys. Rev. Lett. **95**, 010402 (2005).

[52] A. Buchleitner, D. Delande, and J. Zakrzewski, Non-dispersive wave packets in periodically driven quantum systems, Phys. Rep. **368**, 409 (2002).

[53] A. J. Lichtenberg and M. A. Lieberman, *Regular and Chaotic Dynamics* (Springer, Berlin, 1992).

[54] B. J. Dalton, J. Jeffers, and S. M. Barnett, *Phase Space Methods for Degenerate Quantum Gases* (Oxford University Press, Oxford, 2015).

[55] P. Ribeiro, J. Vidal, and R. Mosseri, Exact spectrum of the Lipkin-Meshkov-Glick model in the thermodynamic limit and finite-size corrections, Phys. Rev. E **78**, 021106 (2008).

[56] G. Mazza and M. Fabrizio, Dynamical quantum phase transitions and broken-symmetry edges in the many-body eigenvalue spectrum, Phys. Rev. B **86**, 184303 (2012).

[57] B. J. Dalton and S. Ghanbari, Two mode theory of Bose-Einstein condensates: Interferometry and the Josephson model, J. Mod. Opt. **59**, 287 (2012).